ARTICLE TYPE

1,2,4-Triazolium perfluorobutanesulfonate as an archetypal pure protic organic ionic plastic crystal electrolyte for all-solid-state fuel cells†‡

Jiangshui Luo,[*a,b] **Annemette H. Jensen,**[c] **Neil R. Brooks,**[d] **Jeroen Sniekers,**[d] **Martin Knipper,**[e] **David Aili,**[c] **Qingfeng Li,**[*c] **Bram Vanroy,**[f] **Michael Wübbenhorst,**[f] **Feng Yan,**[g] **Luc Van Meervelt,**[d] **Zhigang Shao,**[h]
5 **Jianhua Fang,**[i] **Zheng-Hong Luo,**[i] **Dirk E. De Vos,**[*b] **Koen Binnemans**[*d] **and Jan Fransaer**[*a]

1,2,4-Triazolium perfluorobutanesulfonate (**1**), a novel, pure protic organic ionic plastic crystal (POIPC) with a wide plastic crystalline phase, has been explored as a proof-of-principle anhydrous proton
10 conductor for all-solid-state high temperature hydrogen/air fuel cells. Its physicochemical properties, including thermal, mechanical, structural, morphological, crystallographic, spectral, and ion-conducting properties, as well as fuel cell performances, have been studied comprehensively in both fundamental and device-oriented aspects. With superior thermal stability, **1** exhibits crystal (phase III), plastic crystalline (phase II and I) and melt phases successively from −173 ℃ to 200 ℃. Differential scanning calorimetry
15 and temperature-dependent powder X-ray diffraction (XRD) measurements together with polarized optical microscopy and thermomechanical analysis reveal the two solid–solid phase transitions of **1** at 76.8 ℃ and 87.2 ℃ prior to the melting transition at 180.9 ℃, showing a wide plastic phase (87 ℃ − 181 ℃). Scanning electron microscopy displays the morphology of different phases, indicating the plasticity in phase I. Single-crystal XRD studies reveal the molecular structure of **1** and its three-
20 dimensional N−H $\cdots$ O hydrogen bonding network. The influence of the three-dimensional hydrogen bonding network on the physicochemical properties of **1** has been highlighted. The temperature dependence of hydrogen bonding is investigated by variable-temperature infrared spectroscopy. The sudden weakening of hydrogen bonds at 82 ℃ seems to be coupled with the onset of orientational or rotational disorder of the ions. The temperature dependence of ionic conductivity in the solid and molten
25 states is measured *via* impedance spectroscopy and current interruption technique, respectively. The Arrhenius plot of the ionic conductivity assumes a lower plateau region (phase I, 100−155 ℃) with a low activation energy of ~36.7 kJ mol^{-1} (*i.e.* ~0.38 eV), suggesting likely a Grotthuss mechanism for the proton conduction. Variable-temperature infrared analysis, optical morphological observations, and powder XRD patterns further illustrate the structural changes. Electrochemical hydrogen pumping tests
30 confirm the protonic nature of the ionic conduction observed in the lower plateau region. Finally, measurements of the open circuit voltages (OCVs) and the polarization curves of a dry hydrogen/air fuel cell prove the long-range proton conduction. At 150 ℃, a high OCV of 1.05 V is achieved, approaching the theoretical maximum (1.11 V).

Broader context

35 The ever-increasing need for efficient energy production and storage urges the development of electrolyte materials for electrochemical devices ranging from fuel cells and dye-sensitized solar cells for electricity generation to lithium-ion batteries and supercapacitors for energy storage. Among various electrolytes, proton conductors are crucial materials for polymer electrolyte membrane fuel cells (PEMFCs). In particular, high temperature PEMFCs, which work in the temperature range of 100−200 °C, are more beneficial than the widespread PEMFCs based on hydrated Nafion® membranes. However, the state-of-the-art high temperature PEMFCs involve liquid electrolytes (*e.g.* H$_3$PO$_4$), and thus suffer from leakage and long-term instability. Consequently, suitable solid-state proton conductors are
40 urgently needed for the development of practical high temperature PEMFCs. Here, with 1,2,4-triazolium perfluorobutanesulfonate as an archetypal example, it is demonstrated as "proof of principle" that protic organic ionic plastic crystals (POIPCs) with a wide plastic crystalline phase are a type of new, promising anhydrous solid-state proton conductors for all-solid-state fuel cells. It is anticipated that POIPCs may also find applications in other electrochemical devices (e.g. sensors).

Introduction

Fuel cells, in particular, polymer electrolyte membrane fuel cells

(PEMFCs), are attractive electrochemical devices both for automobile and stationary applications due to their high energy conversion efficiencies and low emissions.[1] One of the key materials of a PEMFC is the electrolyte, which is a proton conductor for proton transfer from the anode to the cathode. In particular, high temperature PEMFCs operating between 100 ℃ and 200 ℃ offer further benefits such as improved electrode kinetics, simpler water and heat management, and better tolerance to fuel impurities, leading to higher overall system efficiencies.[2]

However, the electrolytes for state-of-the-art high temperature PEMFCs rely on immobilized liquids such as H_3PO_4 and protic ionic liquids[2–7] and thus suffer from leakage and long-term instability. Therefore, all-solid-state PEMFCs based on anhydrous solid-state proton conductors are preferred from the perspective of fabrication, maintenance and durability of the devices.[8–13] One interesting approach is the development of solid acid fuel cells utilizing solid acids (*e.g.* $CsHSO_4$) as the electrolytes and operating at temperatures above their superprotonic phase transitions.[8,9] Drawbacks of these solid acid electrolytes include the narrow temperature window of the superprotonic phase, poor thermal stability, requirement of humidity for stabilization, and difficulties for the preparation of thin films from the inorganic rigid particles.[8,9] In addition, the novel coordination-network-based proton conductors with inherent proton conductivity exhibit poor open circuit voltages (OCVs, *e.g.* ~0.5 V at 130 ℃) for hydrogen/air fuel cells due to fuel crossover related to their inherent porosity.[11,12]

Organic ionic plastic crystals (OIPCs) have emerged as novel solid–state ion conductors.[14–16] They are a type of mesophases (*i.e.* a state of matter intermediate between liquid and solid), in which mobile ions are orientationally and rotationally disordered (a rotator phase) while their centers are located at the ordered sites in the crystal structure. They have various forms of disorder due to one or more solid−solid phase transitions below the melting point and have therefore plastic properties and good mechanical flexibility as well as improved electrode|electrolyte interfacial contact.[14–17] Physically, the structural disorder of their plastic crystalline phases allows for high intrinsic ionic conductivity. Meanwhile, they exhibit other desirable properties such as non-flammability, negligible volatility, high thermal stability, and wide electrochemical windows.[14–16]

While OIPCs have been intensively applied in lithium-ion batteries and dye-sensitized solar cells,[18,19] they are mostly aprotic in nature and are thus not proton conductors. In contrast, reports on OIPCs as proton conductors for fuel cells have received far less attention.[15] The proton-conducting plastic crystals (including OIPCs) in the literature are mainly doped plastic crystals, using acids (*e.g.* CF_3SO_3H), bases, or protic ionic liquids as the dopants for doping the matrix of a certain neat plastic crystal (*e.g.* succinonitrile or choline triflate).[20–22] Similar to conventional high temperature PEMFCs based on H_3PO_4-doped polybenzimidazole membranes,[2] these doped plastic crystals may still degrade over time by gradual release of liquid dopants (*e.g.* acids) during fuel cell operations.[15] The matrices of molecular plastic crystals (*e.g.* succinonitrile) may be quite volatile. In addition, the temperature windows in which the reported proton-conducting plastic crystals have uniform plastic crystalline phases mismatch the working temperature range of 100 ℃ − 200 ℃ desirable for PEMFCs.[15,20–22]

Recently, *protic OIPCs* (POIPCs), which are solid protic organic salts formed by proton transfer from a Brønsted acid to a Brønsted base and in essence are protic ionic liquids in the molten state,[23] have been proposed as promising solid-state proton conductors for fuel cells.[13,15,23] The origins of research on protic ionic plastic crystals can be traced back to an investigation of self-diffusion in a plastic crystal of NH_4NO_3 in 1966.[24] However, studies on them (often containing primary ammonium cations) have been focused on their fundamental properties.[25]

So far, POIPCs haven't been applied as electrolytes for high temperature PEMFCs until very recently.[23] We discovered imidazolium methanesulfonate as a POIPC with a high ionic conductivity of 1.0×10^{-2} S cm^{-1} at 185 ℃ but with a narrow plastic crystalline phase between 174 ℃ and 188 ℃.[23] Due to the rare reports on POIPCs as electrolytes for PEMFCs and the attractive features of POIPCs, such as intrinsic proton conductivity and pure plastic crystals, which obviate the need for the addition of a dopant that may be incompatible with the host matrix,[21] POIPCs deserve more careful exploration for the development of practical all-solid-state high temperature PEMFCs.

In this paper, we report 1,2,4-triazolium perfluorobutanesulfonate **1**, $[C_2H_4N_3]^+$ $\{n\text{-}C_4F_9SO_3\}^-$, as a model POIPC with a wide plastic crystalline phase, high protonic conductivity, and high OCVs for fuel cell applications. The physicochemical properties of **1**, including thermal, mechanical, structural, morphological, crystallographic, spectral, and ion-conducting properties, as well as fuel cell performances, have been studied comprehensively in both fundamental and device-oriented aspects.

Experimental

Sample preparation

1 was synthesized by mixing equimolar amounts of 1*H*-1,2,4-triazole ($C_2H_3N_3$, T_{mp} = 120 ℃, T_{bp} = 260 ℃, Acros Organics, 99.5%) and perfluorobutanesulfonic acid (n-$C_4F_9SO_3H$, TCI, 98%), followed by heating at 190 ℃ for 2 h to promote the complete formation of the organic salt. Compound **1** was then purified by evacuating on a vacuum Schlenk line at 190 ℃ for 12 h to eliminate water and the excess base or acid, resulting in dry crystalline powders. Technically, to avoid evaporation of the corrosive acid which may damage the rubber hoses of the Schlenk line, a slight excess of the base, which was then removed on the Schlenk line, was added into the equimolar composition prior to the purification. Using a clean and dry agate mortar and pestle, powders of **1** were ground into fine powders, which were found to be very soft. Crystals of **1** were grown *via* vapor diffusion of solvent diethyl ether into a saturated solution of **1** in solvent acetonitrile, which was a slow crystallization method resulting in single crystals of sufficient quality for analysis by single-crystal X-ray diffraction (XRD).

Water content determination

The water content of **1** was determined to be 3200 ppm, using a coulometric Karl Fischer moisture titrator.

Infrared analysis

The infrared (IR) spectrum for powders of **1** at room temperature was recorded on a Bruker VERTEX 70 FT-IR spectrometer with a Platinum ATR accessory by accumulating 32 scans at a resolution of 4 cm^{-1}.

Variable-temperature FT-IR measurements were carried out from 28 ℃ to 190 ℃ in a nitrogen atmosphere using a Varian 670-IR FT-IR spectrometer equipped with an FT-IR imaging microscope (with a 15× objective lens) and a Linkam THMS600 heating microscope stage. The sample, which was a single crystal of **1**, was focused on by the imaging microscope and thermally equilibrated at each temperature (accuracy: ± 0.1 ℃) for at least 15 min (unless otherwise specified) prior to the measurements. From 28 ℃ to 70 ℃, the heating rate was 5 ℃ min^{-1} between two consecutive temperatures and was adjusted to 1 ℃ min^{-1} from 70 ℃ onwards. The scan type was transmittance through a KBr window with 64 scans per spectrum and a resolution of 4 cm^{-1} in the range of 4000−700 cm^{-1}.

Raman measurements

A WITec Project system with a 785 nm laser source was used to collect the Raman spectra of **1** and 1*H*-1,2,4-triazole at 30 ℃. The sample of **1** used for Raman spectral analysis was a pellet prepared by pressing fine powders of **1** at around 18 MPa for 30 s.

Thermogravimetric analysis (TGA)

TGA was performed in a nitrogen atmosphere on a thermogravimetric analyzer (AutoTGA 2950HR V5.4A, TA Instruments) using platinum pans at a heating rate of 5 ℃ min^{-1}. The onset temperature of weight loss was used as the decomposition temperature (T_d).

Isothermal gravimetric analysis (IGA) experiments were conducted on the same instrument under an argon atmosphere (60 mL min^{-1}) for 5 h for (*i*) imidazole at 80 ℃ and 150 ℃, (*ii*) 1*H*-1,2,4-triazole at 110 ℃ and 150 ℃, and (*iii*) **1** at 150 ℃, respectively. Prior to IGA tests, the samples were heated to the target temperatures at a heating rate of 20 ℃ min^{-1}.

Thermomechanical analysis (TMA)

TMA was carried out on a TA Instruments TMA Q400 V7.4 Build 93 to study the dimensional change of cylindrical pellets of **1**, which were prepared by uniaxial pressing of fine powders of **1** in a 10 mm diameter metal die under 20 kN (corresponding to a pressure of 255 MPa) for 1 min. The argon flow was 20.0 mL min^{-1}. The temperature range was from room temperature to 120 ℃ with a ramp of 0.2 ℃ min^{-1}. The density of the cylindrical dense pellet of **1** prior to the thermomechanical analysis was obtained by dividing the mass by the corresponding volume. The measured density is 1.82 g cm^{-3} at room temperature, agreeing well with the calculated density of 1.842 g cm^{-3} at 27 ℃ for a single crystal of **1** and thus proving the dense state of as-prepared pellets of **1**.

Differential scanning calorimetry (DSC)

DSC measurements were conducted on a TA Instruments DSC Q2000 V24.4 Build 116 purged with nitrogen. Samples were in the form of fine powders or cylindrical dense pellets of **1**. The pellets were prepared by pressing fine powders of **1** in a 5 mm diameter metal die under 20 kN for 1 min and then applying a hydraulic press of 300 MPa for 1 min. TA Instruments T$_{zero}$ aluminum hermetic pans were used to tightly seal the samples. The sample mass was around 19 mg for fine powders and 45 mg for pellets, respectively. For the powder samples, after the samples were held at −40 ℃ for 3 min, they were heated from −40 ℃ to 200 °C and then cooled to −150 ℃, followed by another two repeated thermal cycles (*i.e.* −150 ℃ → +200 ℃ → −150 ℃ → +200 ℃ → 20 ℃) at heating/cooling rates of 5 ℃ min^{-1}. The first and second heating scans as well as the first cooling scan were performed to eliminate the effects of thermal history of the samples. DSC thermograms recorded during the second cooling and the subsequent third heating scans were used to obtain the phase transition temperatures and other parameters presented here. Similarly, for the cylindrical pellet samples, after being held at −40 ℃ for 3 min, they were heated from −40 ℃ to 200 °C and then cooled to −40 ℃, followed by another two repeated thermal cycles at heating/cooling rates of 2 ℃ min^{-1}. DSC thermograms recorded during the second cooling and the subsequent third heating scans were also used.

X-ray diffraction (XRD)

Temperature-dependent powder XRD for fine powders of **1** was recorded in an argon atmosphere from 25 ℃ to 160 ℃ on a powder X-ray diffractometer (X'Pert PRO, PANalytical) using Cu Kα radiation (λ = 1.5406 Å) to identify solid–solid phase transitions. Measurements were done in a high-temperature oven chamber (HTK 1200N, Anton Paar) using an Al$_2$O$_3$ sample holder for the HTK chamber. The heating element installed is a Kanthal APM (Cr: 22%; Al: 5.8%; Fe: rest) and the thermocouple is a Pt-10%Rh-Pt sensor (type S). The sample was stabilized at each measurement temperature (accuracy: ±1 ℃) for 10 min before each measurement. The temperature ramp between two consecutive temperatures was 1 ℃ min^{-1}. Each measurement consisted of a θ−2θ scan from 5 °to 50 °with a step size of 0.026 ° and a scan speed of 0.011 °s^{-1}.

In addition, powder XRD measurements were performed for fine powders of **1** on the same X-ray diffractometer but in the normal chamber with air atmosphere at 25 ℃. The sample was stabilized at 25 ℃ for 30 min before the measurement, which consisted of a θ−2θ scan from 5 °to 80 °with a step size of 0.052 ° and a scan speed of 0.013 °s^{-1}.

Crystal structure determination

Single-crystal XRD measurements were carried out on an Agilent SuperNova diffractometer at −173 ℃ (100 K) and 27 ℃ (300 K) successively for a single crystal of **1** using Mo Kα radiation (λ = 0.71073 Å). The structure was solved with SHELXS-97 and then refined with SHELXL-97 while the molecular graphics were drawn and exported using Olex2.[26] The position of the hydrogen atoms attached to carbon were placed in calculated positions and refined as riding with $U_{iso}(H) = 1.2 \times U_{eq}(C)$, whilst those attached to nitrogen were found in the difference electron density map and the N−H distances restrained to be 0.86(1) Å, whilst the thermal parameters of the hydrogen atoms were allowed to freely refine. Crystallographic information files are provided in the Supporting Information†.

Morphological observations

An environmental scanning electron microscope (SEM) XL30 ESEM FEG (FEI) was employed to observe the morphology of

cross sections of a plate (formed by natural solidification of melts of **1** in air) or a fractured pellet of **1** at different temperatures under a vacuum of around 3.0 Torr (*i.e.* ~400 Pa). All images were acquired with an acceleration voltage of 25.0 kV. Polarized ₅ optical microscopy was used to exclude the possibility of partial melting of **1** at around 77 ℃ and 87 ℃.

Conductivity measurements

The ionic conductivity of **1** in molten state was measured in a two-electrode cell, using a current interruption technique with a ₁₀ symmetric square wave current (frequency: 6.6 kHz). The cell was made of a round hollow polytetrafluoroethylene (PTFE) tube with a length of 2.5 cm and an inner diameter of 1.1 cm. Platinum foils were attached to both ends of the cell through which the current was supplied and between which the voltage drop was ₁₅ measured. The cell was filled with **1** and then heated to 190 ℃. More salt was added until the cell was completely filled with molten salt. The cell was cooled to 185 ℃ for the first measurement and the temperature was thereafter increased to 190 ℃, 195 ℃ and 200 ℃ successively.

₂₀   To measure the ionic conductivity of **1** in solid state, cylindrical pellets of **1** with a diameter of 13 mm were prepared by pressing fine powders of **1** at around 3000 kg cm^{-2} (*i.e.* 294 MPa) for 3 min. Each side of the pellet was uniformly painted with a thin layer of silver paste (Loctite® 3863, Henkel Co.) to ₂₅ enhance the contact between the pellet and the electrodes. The conductivity was measured by the two-electrode AC impedance technique using a Princeton Potentiostat VersaSTAT 4 equipped with VersaStudio software in the frequency range from 1 Hz to 300 kHz at temperatures ranging from 65 ℃ to 180 ℃ under ₃₀ ambient air at an interval of 5 ℃. At each temperature, it was stabilized for 10 min prior to the measurement.

  For the measurements of samples of **1** in both molten and solid states, the ionic conductivity, σ (S cm^{-1}), was calculated according to eqn (1):

₃₅ $$\sigma = d/(R \times S) \tag{1}$$

where d is the thickness of the electrolyte or the distance between the measuring electrodes (cm), S the geometric area of the electrolyte (cm^2), and R the measured resistance of the electrolyte (Ω).

₄₀ **Electrochemical hydrogen pumping tests**

Cylindrical pellets of **1** with a diameter of 20 mm and a thickness of around 0.5 mm were prepared by pressing fine powders of **1** at around 3000 kg cm^{-2} for 3 min. A cell was assembled with two electrodes prepared from Pt/C catalysts (60 wt%, home-made) on ₄₅ each side of an electrolyte pellet. The diameter of the electrode area is 13 mm. Dry hydrogen gas (flow rate: 50 ml min^{-1}) was flowing on both sides of the cell. At 150 ℃ the cell voltage was virtually 0 V (± 2 mV). Constant DC voltages of 1.0 V and 0.50 V were applied between the two electrodes successively. The ₅₀ corresponding time dependence of the current through the cell was recorded simultaneously. During the chronoamperometric measurement under DC voltage of 0.50 V, the hydrogen flow was switched to argon for both sides for about 130 s before hydrogen flow was restored.

₅₅ **Fuel cell evaluations**

Cylindrical pellets of **1** with a diameter of 13 mm and a thickness of 1.0 mm were prepared by pressing fine powders of **1** at around 3000 kg cm^{-2} for 3 min. The pellet was used as the electrolyte and assembled with electrodes (contact surface area: 0.50 cm^2) ₆₀ made from Pt/C catalysts (60 wt%, home-made) on each side to form a single cell. High platinum loading (7 mg Pt cm^{-2}) on each side was used because the contact between electrolyte and electrode had not been optimized. The single cell was supplied with pure hydrogen gas and dry decompressed air with ambient ₆₅ back pressure at the anode and the cathode, respectively. The polarization curves were measured from 120 ℃ to 180 ℃ by linear sweep voltammetry at a scan rate of 10 mV s^{-1}.

Results and discussion

Thermal, structural and morphological analysis

₇₀ The complete formation of the organic salt of compound **1** (Fig. 1) is indicated by the infrared absorption bands at 1571 and 1562 cm^{-1}, which are due to the protonation of 1*H*-1,2,4-triazole molecules,[27a] and the fact that no traces of the precursors (acid or base) have been detected (Fig. S1, S2 and S3†). In the region of ₇₅ 3350−2750 cm^{-1}, the broadening of the bands can be attributed to the hydrogen bonding network,[27−30] corroborating the findings from single crystal data of **1** described later.
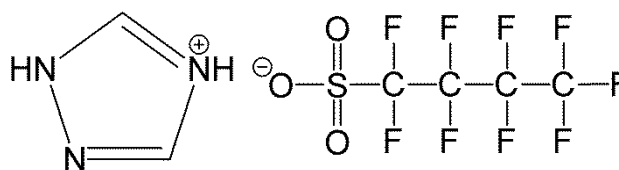

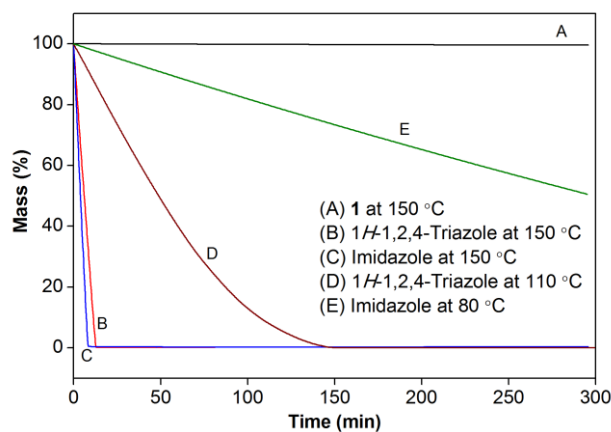**Fig. 1** Chemical structure of the proton conductor **1**.

₈₀ **Fig. 2** Isothermal gravimetric analysis of (A) **1** at 150 ℃, (B) 1*H*-1,2,4-triazole at 150 ℃, (C) imidazole at 150 ℃, (D) 1*H*-1,2,4-triazole at 110 ℃, and (E) imidazole at 80 ℃ in Ar atmosphere. Note that the melting point for 1*H*-1,2,4-triazole and imidazole is 120 ℃ and 89 ℃, ₈₅ respectively.

  Compared with model organic molecular proton conductors like imidazole (T_{mp} = 89 ℃, T_{bp} = 256 ℃) and 1*H*-1,2,4-triazole,[31] as well as conventional electrolytes like Nafion® membranes[23] and 85% H$_3$PO$_4$,[32] **1** showed superior thermal ₉₀ stability and negligible vapor pressure (Fig. 2). Clearly, the negligible volatility of **1** as a solid-state proton conductor renders it more suitable than molecular species for long-term device use.

Thermogravimetric analysis (Fig. S3†) recorded in nitrogen at a heating rate of 5 ℃ min⁻¹ reveals the decomposition temperature to be as high as 291 ℃. **1** is also thermally stable in air (Fig. S4†).
Moreover, 1,2,4-triazolium cations and perfluorobutanesulfonate
5 anions have been shown to have adequate electrochemical stability on platinum working electrodes.[27a,33]
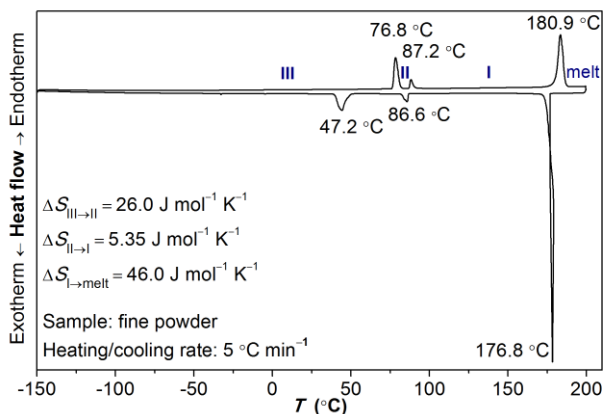

Fig. 3 DSC thermograms of **1** in the form of fine powders measured at
10 5 ℃ min⁻¹ for both the heating and cooling scans. The onset temperatures and entropy changes for each phase transition in the heating scan are given. Each solid phase is labeled by Roman numerals with the highest temperature solid phase denoted by phase I. The melt phase is also indicated. The peak temperature for the first endothermic transition is 78.4 ℃.

15 **Table 1** Onset temperatures (T), enthalpy changes (ΔH) and entropy changes (ΔS) of each phase transition.

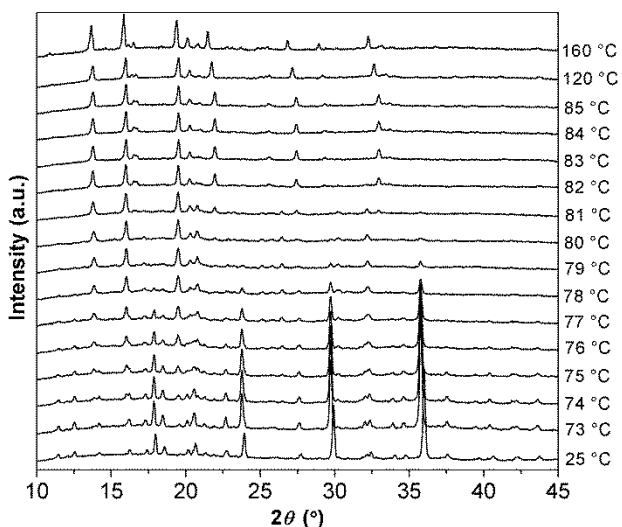| Phase transition	T/ ℃	ΔH/kJ mol⁻¹	ΔS/J K⁻¹ mol⁻¹
III → II	76.8	9.10	26.0
II → I	87.2	1.93	5.35
I → melt	180.9	20.9	46.0

Fig. 4 Powder XRD patterns of fine powders of compound **1** in an argon
20 atmosphere as a function of temperature, demonstrating structural changes with increasing temperature. Before each measurement, the sample was stabilized at each measurement temperature (accuracy: ±1 ℃) for 10 min. The temperature ramp between two consecutive temperatures was 1 ℃ min⁻¹. Cu Kα radiation (λ = 1.5406 Å) was used. Each

25 measurement consisted of a $\theta-2\theta$ scan with a step size of 0.026 ° and a scan speed of 0.011 ° s⁻¹.
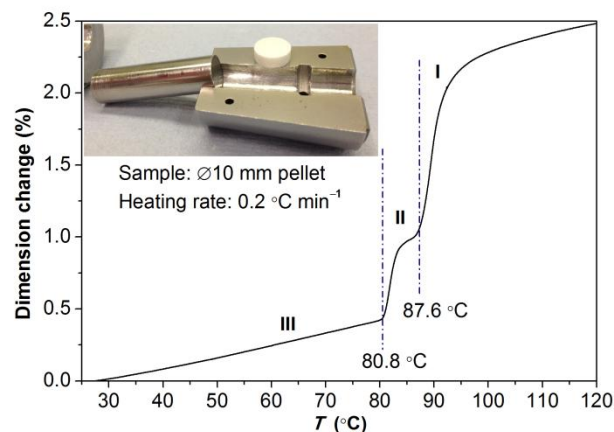

Fig. 5 Temperature dependence of the height change of a cylindrical, dense pellet of **1** (diameter: 10 mm) during heating from room
30 temperature to 120 ℃. The heating ramp was 0.2 ℃ min⁻¹. The onset temperature for each discontinuous dimensional change is given. Dash dotted lines show phase-transition temperatures. Inset: photograph of the pellet and the die used for preparation of pellets.

During the heating scan in the DSC measurements recorded at
35 5 ℃ min⁻¹ (Fig. 3), three distinct endothermic transitions were observed at 76.8 ℃, 87.2 ℃ and 180.9 ℃, respectively, with the last transition corresponding to the melting of **1**. The onset temperature, the enthalpy change, and the entropy change of each phase transition are summarized in Table 1.
40 Temperature-dependent powder XRD measurements (Fig. 4) indicate clearly a transformation between two different crystalline structures and a likely increase in space group symmetry at around 78 ℃, confirming the first endothermic transition (phase III → phase II), whose peak temperature is 78.4 ℃, to be a
45 solid−solid phase transition with an evident entropy change, $\Delta S_{III \to II}$, of 26.0 J K⁻¹ mol⁻¹. In addition, the second endothermic transition (phase II → phase I) at 87.2 ℃ is proved to be another solid−solid phase transition, though with a smaller entropy change, $\Delta S_{II \to I}$, of 5.35 J K⁻¹ mol⁻¹. The sharp reflections suggest
50 that **1** possess long-range-ordered structures in phase I, II and III. While all of the diffraction peaks belonging to the room temperature (phase III) powder XRD pattern completely disappear in phase I (the highest temperature solid phase), the XRD patterns of phase I are observed to be simpler, implying a
55 higher symmetry space group and phase I as a plastic phase.[23,25,34−37] The reduction of diffraction peaks in phase I indicates the presence of dynamic rotational disorder which leads to the plastic properties. As the 1,2,4-triazolium cation is smaller in size and has smaller inertia momentum than the long
60 perfluorobutanesulfonate anion, very likely it is the cationic moieties that are orientationally disordered. Furthermore, observations by polarized optical microscopy excluded the possibility of partial melting of **1** at 77 ℃ and 87 ℃ (Fig. S5†). Therefore, it is concluded that **1** is a POIPC with a uniform and
65 consistent plastic crystalline state in a wide temperature range (e.g. 87 ℃ − 160 ℃) without any phase transitions. Notably, plastic crystals based on perfluorobutanesulfonate anions have seldom been reported,[33] although the range of anions and cations utilized in the synthesis of plastic crystal phases continues to
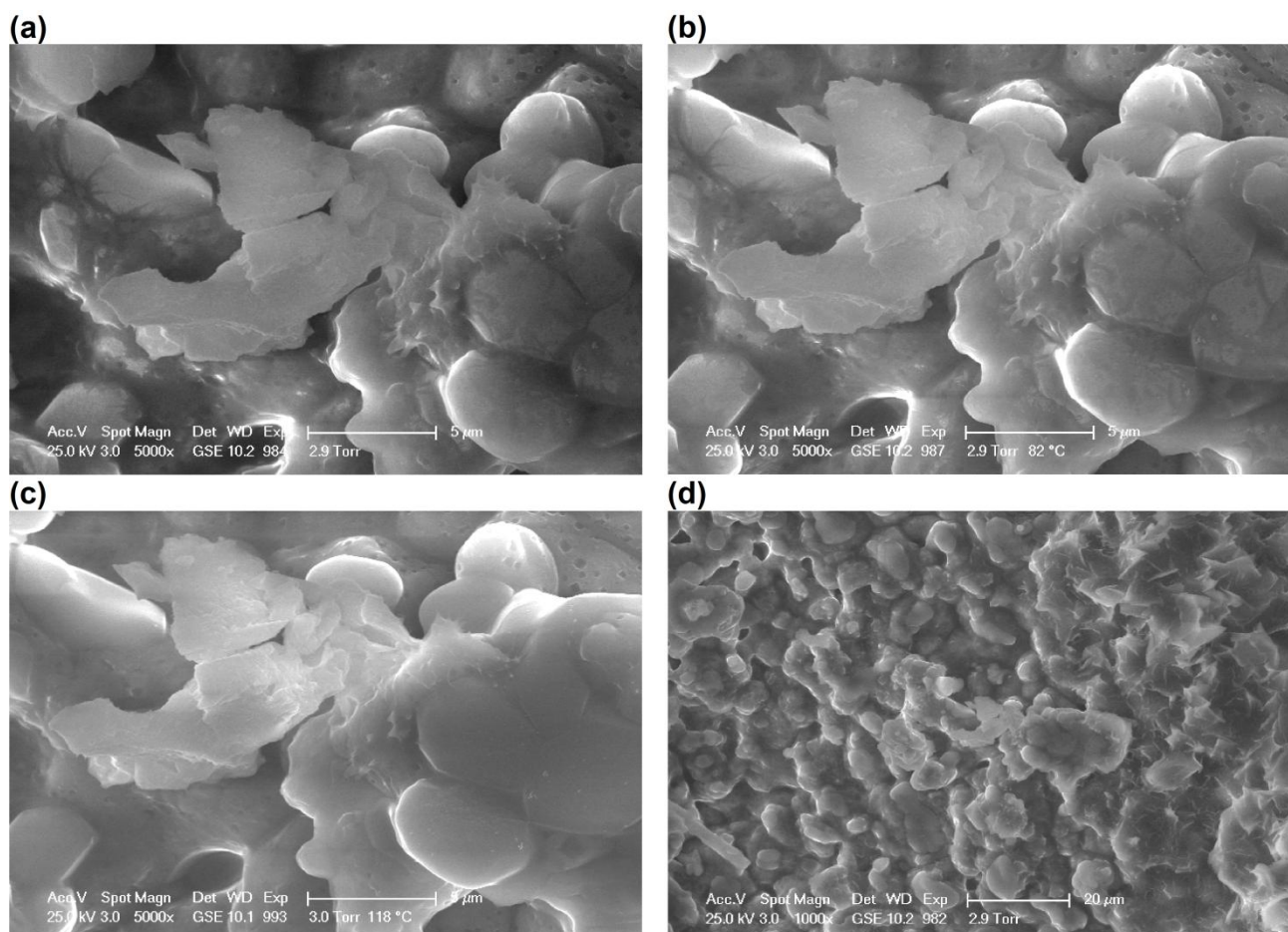
Fig. 6 SEM images of fracture surface. Grain sizes and grain boundaries at (a) room temperature, (b) 82 ℃ and (c) 118 ℃, corresponding to phase III, II and I, respectively. (d) Waxy fracture surface at room temperature. The fracture surface was formed by breaking a pressed dense pellet of **1** with a hammer after liquid nitrogen quench. The pellet was prepared by uniaxial pressing of fine powders.

increase.[15] Furthermore, the thermal behavior (*e.g.* wide plastic phase) of **1** is rare for reported POIPCs and other proton-conducting neat ionic plastic crystals.[11,23–25,36] The high melting point is another merit of **1** as a solid-state proton conductor for high temperature PEMFCs because the majority of the reported OIPCs exhibit melting points below 120 ℃,[14–16,18–22,34–38] which is insufficient for the operating temperature range of all-solid-state high temperature PEMFCs.

The entropy of fusion, ΔS_f, at the melting point of 180.9 ℃ is calculated to be 46.0 J K^{-1} mol^{-1} ($\Delta S_f = \Delta H_f/T_m$). For molecular plastic crystals ΔS_f is very low (typically < 20 J K^{-1} mol^{-1}).[17] However, for an OIPC, which contains two different ions, ΔS_f may be > 20 J mol^{-1} K^{-1}, as is observed for a number of OIPCs.[23,34,35,38] Likely, the cations are highly disordered in phase I and are hence the origin of the plasticity while the large anions of **1** may exhibit less disorder in phase I. Therefore, significant entropy, which is to be released on melting, remains in phase I. While a completely free rotation would result in a highly symmetric plastic phase (often cubic) for the high temperature plastic phase,[25a,35,39,40] the plastic phase of **1** seems to have a symmetry which is lower than that of the cubic plastic phases, further implying a less free rotational motion of the ions, which may be limited to rotations around specific symmetry axes.[40]

The thermal expansion of a pressed dense pellet of **1** is relatively uniform except for the sudden jumps during the plastic transitions (Fig. 5). Obviously, the two solid-solid phase transitions are both discontinuous as determined from the jumps in dimensional change along the height of the cylindrical pellet. The onset temperatures for the two discontinuous dimensional changes are 80.8 ℃ and 87.6 ℃, respectively, which are in line with the onset temperatures of corresponding endothermic peaks in the DSC curves (Fig. 3, Fig. S6 and S7†). The solid-solid phase transitions of OIPCs in the form of single crystals and bulk materials have also been shown to be accompanied by evident dilation for all axes and volume expansion, respectively.[25b,41] The abrupt thermal expansion reflects the onset of rotational motion of cations or anions and hence lattice transformation of **1**, resulting in the onset of plasticity for **1**.[40,42]

To further examine the plasticity of **1**, variable-temperature SEM was employed to observe the microstructure of **1** at different temperatures. As shown in the SEM images of a plate formed by natural solidification of melted samples of **1**, periodic slip planes and steps emerge on the fracture of the plate at 25 ℃, 82 ℃ and 121 ℃ (Fig. S8a, S8b and S8c†), respectively. At 28 ℃, the normal surface of the plate shows distinct slip planes (Fig. S8d†), proving predominant plasticity, which have also

been observed in SEM images of some aprotic OIPCs.[14,16,43–45] Moreover, plasticity is believed to be associated with the process of slip along favorable crystallographic orientations.[44,45] Compared with some pyrrolidinium-based OIPCs,[43] which show brittle features and sharp edges on their fracture surfaces, **1** seems to be "softer". In fact, **1** was so soft that a conductivity cell with glass as the shaft material was still in a perfect state after an attempt of using it to measure the ionic conductivity of **1** in the solid state. Furthermore, the fracture surface of a pellet of compound **1** prepared by uniaxial pressing of fine powders shows that the grain boundaries become less resolved when the temperature is raised from room temperature to 118 ℃ (Fig. 6a, 6b and 6c), revealing the thermal-induced plastic deformation in the pellet of **1**, whose grains have already experienced strong compressive stresses during uniaxial pressing. This plastic deformation is correlated with the thermomechanical analysis results (Fig. 5), which shows significant dimensional change of the pellet upon the two solid-solid phase transitions from room temperature to 120 ℃. Such plastic deformation may accommodate thermal-induced volume changes in fuel cell applications. Additionally, the fracture surface looks rather waxy even at room temperature (Fig. 6d). The high plasticity of compound **1** is largely attributed to its inherent short-range rotational disorder embedded in a long-rang ordered crystalline structure,[16] implying relatively easy motion of ions within the material, which is consistent with the subsequent ionic conductivity data. The Supporting Information† gives more detailed infrared, thermal, and structural (Fig. S9 and S10†) analysis.

Crystal structure and hydrogen bonding

The crystal data of **1** are listed in Table 2. To the best of our knowledge, it is the first report on the crystal structure of a perfluorobutanesulfonate-based salt which exhibits ionic plastic crystalline behavior.[33,46,47] The crystal has similar unit cell parameters at the two temperatures except for differences caused by thermal expansion/contraction (Fig. 7 and Table 2).

The structure consists of one cation and one anion in the crystallographic asymmetric unit. The two N−H groups of the 1,2,4-triazolium cation are involved in hydrogen bonds with three neighbouring perfluorobutanesulfonate anions (Table 3 and Fig. S11†). These hydrogen-bonding interactions create two-dimensional sheets of anions and cations in the *ab* plane (Fig. 8 and Fig. S12†). Adjacent planes stack inverted such that the perfluorobutyl chains from adjacent layers interdigitate and such that an anion from one plane lies opposite a cation from an adjacent plane. Hence, the overall packing is layered along the crystallographic *c*-axis with the negative $-SO_3^-$ and positive 1,2,4-triazolium regions alternating with perfluorobutyl chain regions. While the fluorine segregation seems to be one important factor dominating the crystal packing, the segregation of the ionic parts from the fluorous tails has also been seen in some perfluorobutanesulfonates.[46]

As can be seen from the displacement ellipsoids the thermal motion at 27 ℃ (Fig. 7b) is much greater than that at −173 ℃ (Fig. 7a). Additionally, the thermal motion within the hydrogen-bonded part of the structure (1,2,4-triazolium cation and $-SO_3^-$ moiety) is lower than in the perfluorobutyl chains. Furthermore, as can be expected, the thermal motion increases towards the end

of the perfluorobutyl chain. At 27 ℃, the thermal ellipsoids are so large that it was worth considering if the perfluorobutyl chains should be modelled and refined as disordered entities; however, this approach did not improve the quality of the refinement and just introduced unnecessary extra parameters and restraints. In addition, the powder XRD pattern of fine powders of **1** measured at 25 ℃ under air atmosphere agrees very well with those calculated from the single crystal data of **1** (Fig. 9), indicating that the single crystal structure is representative of the entire sample and further demonstrating the complete formation of compound **1**.

Table 2. Crystallographic data of **1** at 100 K (−173 ℃) and 300 K (27 ℃).

| Chemical formula	$C_6H_4F_9N_3O_3S$	$C_6H_4F_9N_3O_3S$
Formula weight	369.18	369.18
CCDC number	1013012	1013013
T/K	100(2)	300(2)
Wavelength/Å	0.71073	0.71073
Crystal system	Monoclinic	Monoclinic
Space group	$P2_1/n$	$P2_1/n$
a/Å	5.2742(4)	5.3510(3)
b/Å	8.2719(5)	8.2492(5)
c/Å	29.673(2)	30.2383(18)
α/ °	90	90
β/ °	93.124(7)	93.950(5)
γ/ °	90	90
V/Å³	1292.66(16)	1331.59(13)
Z	4	4
ρ_{calc}/g cm⁻³	1.897	1.842
μ/mm⁻¹	0.379	0.367
Absorption correction	Multi-scan	Multi-scan
θ range/ °	2.82 to 29.04	2.81 to 29.14
Reflections collected	5308	6146
Independent reflections	2930	3066
R_{int}	0.0234	0.0208
Parameters	207	207
Goodness-of-fit on F^2	1.190	1.142
R_1, wR_2 [$I > 2\sigma(I)$]	0.0559, 0.1163	0.0906, 0.2334
R_1, wR_2 (all data)	0.0617, 0.1193	0.1009, 0.2404

(a)

(b)
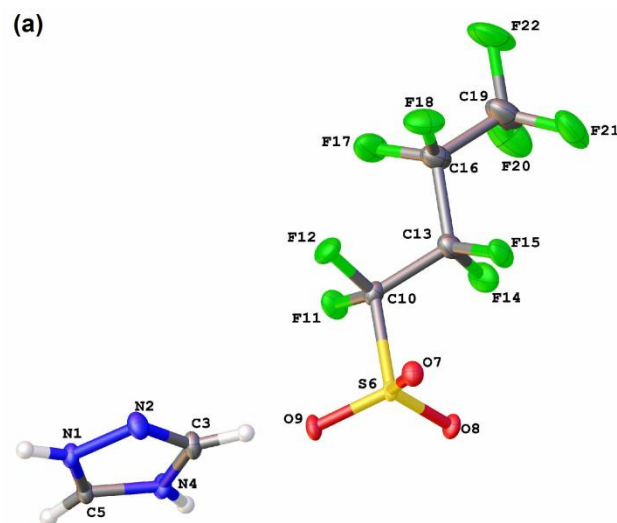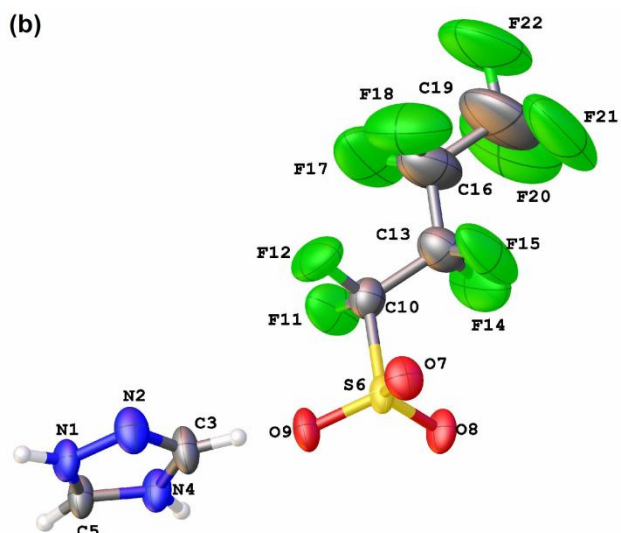
Fig. 7 Molecular structure of **1** with the atom-numbering scheme, showing 50% probability displacement ellipsoids at (a) −173 ℃ and (b) 27 ℃, respectively. H atoms are drawn as spheres of arbitrary size (C: grey; H: white; F: green; N: blue; O: red; S: yellow).

Table 3 Hydrogen bond geometry parameters for **1** at −173 ℃ and 27 ℃.

T/ ℃	H-bond	H···O/Å	N···O/Å	∠N−H···O/ °
−173	N1−H1···O7^i	2.45(3)	3.038(3)	126(3)
	N1−H1···O8^{ii}	2.03(2)	2.775(3)	145(4)
	N4−H4···O9^{iii}	1.993(19)	2.776(3)	151(3)
27	N1−H1···O7^i	2.51(6)	3.053(5)	122(5)
	N1−H1···O8^{ii}	2.04(4)	2.805(4)	148(6)
	N4−H4···O9^{iii}	1.99(3)	2.791(5)	154(6)

Symmetry codes: ^{i} −1+x,−1+y,z; ^{ii} x,−1+y,z; ^{iii} −1+x,y,z
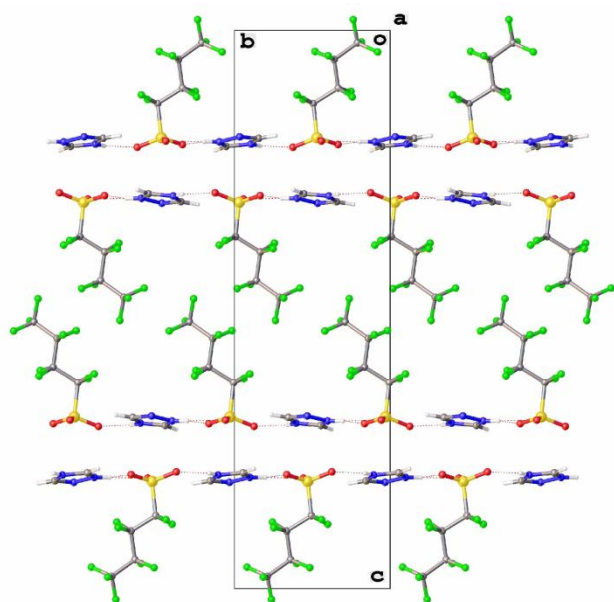
Fig. 8 View of the packing in the crystal structure of compound **1** at −173 ℃ (C: grey; H: white; F: green; N: blue; O: red; S: yellow).

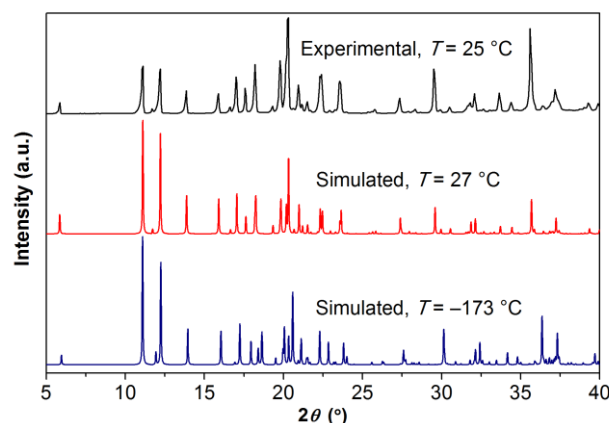**Fig. 9** Comparison of the experimental powder XRD pattern of fine powders of **1** at 25 ℃ in air in the normal chamber of the X-ray diffractometer used (top) with those simulated from the crystal data of compound **1** determined at 27 ℃ (middle) and −173 ℃ (bottom). For the powder XRD measurement, step size: 0.052 °; scan speed: 0.013 °s^{-1}.

Resembling the distinct difference between protic ionic liquids and aprotic ionic liquids,[27,29,48] the three-dimensional N−H···O hydrogen bonding network (Table 3 and Fig. S11†) demonstrates that the key property that distinguishes POIPCs from aprotic OIPCs is the proton transfer from the Brønsted acid to the Brønsted base, leading to the presence of proton-donor and proton-acceptor sites and the formation of a strong hydrogen bonding network. Raman spectroscopic analysis further confirms the strong hydrogen bonding network as indicated by the low-frequency vibrational modes at 71, 109, 147 and 178 cm^{-1} (Fig. S2†), which may be assigned to the intermolecular bending and stretching modes of the hydrogen bonds $^+$N−H···O$^-$.[30,48,49] The three significant N−H···O hydrogen bonds shown in Table 3 all exhibit H···O lengths well within the sum of the van der Waals radii ($r_H + r_O$ = 2.70 Å).[50] In particular, the hydrogen bond of N4−H4···O9 shows the shortest H···O length (1.99 Å) and the largest angle (151 °) at −173 ℃, revealing a relatively short and directional interaction. In addition, similar to the N−H···N hydrogen bonds in a single crystal of 1*H*-1,2,4-triazole,[30] the N−H···O hydrogen bonds in the single crystal of compound **1** are also temperature sensitive and become slightly longer when the temperature increases from −173 ℃ to 27 ℃ (Table 3).

To further investigate the influence of temperature on hydrogen bonding interactions, variable-temperature FT-IR spectra were recorded for a single crystal of **1** from 28 ℃ to 190 ℃ under a nitrogen atmosphere (Fig. 10 and Fig. S13†). When the temperature was increased from 80 ℃ to 82 ℃, the band at 3234 cm^{-1} representing N−H stretching vibration was shifted to a much higher stretching frequency (Fig. 10a), suggesting the distinct weakening of N−H···O hydrogen bonds, as for organic salts with weakly basic anions A$^-$ (*e.g.* CF$_3$SO$_3^-$), higher N−H stretching frequencies correspond to weaker N−H···A$^-$ hydrogen bonds.[28] In addition, the band at 943 cm^{-1}, attributed as N−H out-of-plane bending of the 1,2,4-triazolium cations,[30] was blue shifted to 957 cm^{-1}. Meanwhile, the bands at 1572 and 1560 cm^{-1} attributed to the protonation of 1*H*-1,2,4-triazole coalesce into a single peak at 1558 cm^{-1} when the crystal was heated from 80 ℃ to 82 ℃ (Fig. 10b), agreeing very well with the phase III → phase II transition as revealed by

thermomechanical analysis (Fig. 5) and temperature-dependent powder XRD patterns (Fig. 4), wherein some diffraction peaks disappear or appear at around 82 ℃. By comparing the infrared spectra of 1-methylimidazolium perfluorobutanesulfonate and 1,2,4-triazolium benzenesulfonate (Fig. S14 and S15†), the two bands at 1419 and 1396 cm^{-1} of the crystal of **1** may be assigned as ring stretching of 1,2,4-triazolium cations[30,33] and were red shifted when the temperature increased from 80 ℃ to 82 ℃. These spectral changes strongly imply the onset of orientational or rotational motion of the 1,2,4-triazolium cations, which is expected to facilitate the cation mobility.
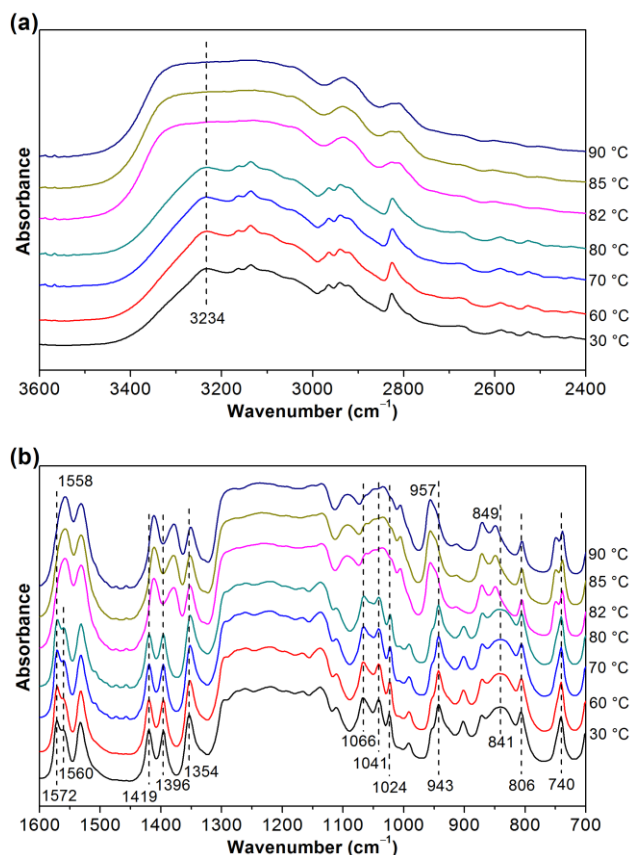
Fig. 10 Variable-temperature FT-IR spectra of a single crystal of **1** under a nitrogen atmosphere in the temperature range of 30−90 ℃: (a) 3600−2400 cm^{-1}; (b) 1600−700 cm^{-1}.

Nevertheless, the peaks at 1354, 806 and 740 cm^{-1} related to the perfluorobutanesulfonate anions remained at the same position. The peaks at 1066, 1041 and 1024 cm^{-1} associated with SO$_3$ symmetric stretching became broadened and less resolved, which should be correlated with the change of hydrogen bonds. The relatively broad vibrational mode at 841 cm^{-1} most likely assigned as S−O stretching,[51] became sharper and was blue-shifted to 849 cm^{-1} when the temperature increased from 80 ℃ to 82 ℃, indicating the strengthening of S−O bonds (or S−O bonds being less restrained) and thus further confirming the weakening of N−H···O hydrogen bonds. Therefore, unlike the gradual decrease of the strength of hydrogen bonds versus the increasing temperature observed in protic ionic liquids,[29] the sudden weakening of hydrogen bonds of **1** at 82 ℃ seems to be coupled with the onset of orientational or rotational disorder of the ions

(most likely 1,2,4-triazolium cations) as well as the onset of abrupt thermal expansion (Fig. 5). This is somewhat similar to the time-resolved infrared spectroscopic study of liquid water, in which rotations and hydrogen bond dynamics are discovered to be strongly coupled.[52]

Furthermore, the significant blue shift of N−H stretching frequency at 3234 cm^{-1} when the temperature increased from 80 ℃ to 82 ℃ implies an abrupt and prominent lengthening of hydrogen bonds,[30] which in essence should be due to more global changes with a longer time scale that involve hydrogen bond breaking and reforming rather than the fast local motions involving mainly small changes in hydrogen bond lengths with some angular changes.[52,53] This may be regarded as a result of the transformation between two different crystalline structures (phase II → phase I) beginning at around 82 ℃ as revealed by the temperature-dependent powder XRD measurements (Fig. 4).

In addition, the correlation of onset of rotation with suddenly weakened hydrogen bonds at around 82 ℃ may also be interpreted in terms of the change of the coefficient of thermal expansion. From the slopes of the temperature dependence of dimensional change of a pressed dense pellet (Fig. 5), it can be seen that the plastic crystalline phases (phase II and phase I) have larger thermal expansion coefficients than the crystalline phase (phase III), which should be attributed to the orientational or rotational disorder in the plastic crystalline phases weakening the interactions between cations and anions and hence allowing a larger thermal expansion.[54]

Ionic conductivity

There are four distinct linear regions for the temperature dependence of the ionic conductivity of **1** (Fig. 11): the ordered crystalline region (phase III, 65−75 ℃), the lower plateau region (phase I, 100−155 ℃), the steep region (phase I, 165−180 °C), and the molten state (185−200 ℃). In particular, the temperature dependence of the ionic conductivity is correlated well with the thermomechanical analysis result of a cylindrical dense pellet (Fig. 5): the linear curve in phase III; the transition from a nonlinear curve (87.6−100 ℃) to a linear curve (above 100 ℃) in phase I.

The Arrhenius plot of the ionic conductivity in the solid state is given in Fig. 12. The activation energies for the four linear regions are calculated using the Arrhenius equation and are listed in Table 4:

$$\sigma = \sigma_0 \exp\left(-\frac{E_a}{RT}\right) \qquad (2)$$

where σ is the ionic conductivity in S cm^{-1}, σ_0 the pre-exponential factor in S cm^{-1} (*i.e.* the maximum ionic conductivity that it would have at infinite temperature), E_a the activation energy in kJ mol^{-1}, R the universal gas constant, and T the absolute temperature in Kelvin. Overall, E_a decreases as **1** is heated through each phase transition, which is in line with the same trend observed in imidazolium methanesulfonate[23] and some aprotic OIPCs[16,35] and reflects the phase-dependent transport properties of **1**. The properties for the linear and non-linear regions are discussed as follows:

(i) Ordered crystalline region (Phase III, 65−75 ℃)
In the ordered phase III, the material has a low ionic conductivity below 1×10^{-8} S cm^{-1}, which is attributed to the fact that the

movement of ions is highly restricted in the relatively rigid lattice. The ionic conductivity is 3.21×10^{-10} S cm^{-1} at 65 ℃ and exhibits a strong temperature dependence. Based on the high value of E_a (228.3 ± 27.5 kJ mol^{-1}) and the ultra-low ionic conductivity, the mechanism for self-diffusion in the ordered crystalline phase III is speculated to be lattice self-diffusion.[14]
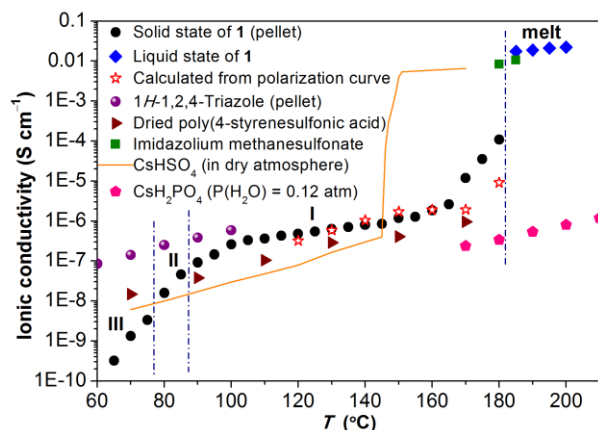

Fig. 11 The ionic conductivity of **1** as a function of temperature. The solid black circles and solid blue diamonds represent the ionic conductivity in the solid state (in the form of a cylindrical dense pellet) and the molten state, respectively. The hollow red asterisks denote the DC protonic conductivities calculated from the slopes (Table S1) of the polarization curves (Fig. 14a) at the corresponding temperatures using Ohm's law. For comparison, the ionic conductivities of 1H-1,2,4-triazole (purple balls),[10] dried poly(4-styrenesulfonic acid) membrane (wine triangles, 5.4 meq g^{-1}),[56a] CsHSO$_4$ (orange solid line),[56c] and imidazolium methanesulfonate (olive square)[23] in the anhydrous solid states are shown. The ionic conductivity of CsH$_2$PO$_4$ (pink pentagon) measured under humidified air with a constant water content of 12 mol% (*i.e.* P(H$_2$O) = 0.12 atm) is also shown.[56e] Dash dotted lines show solid-solid phase transition temperatures of **1**.
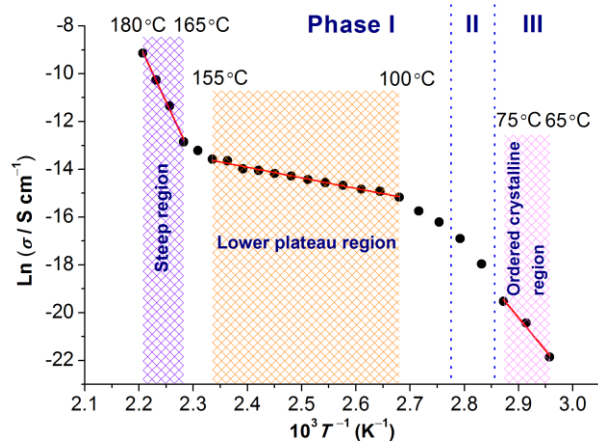

Fig. 12 Arrhenius plot for the ionic conductivity of **1**. Red straight lines represent the fitting results using Arrhenius equation for the respective regions: the ordered crystalline region (phase III, 65−75 ℃), the lower plateau region (phase I, 100−155 ℃) and the steep region (phase I, 165−180 °C). The pellet of **1** was prepared by pressing fine powders of **1** at around 3000 kg cm^{-2} (*i.e.* 294 MPa) for 3 min so that it is comparable to the crystal used for variable-temperature FT-IR measurements in terms of density. Dotted lines show solid-solid phase transition temperatures.

Table 4 Fitting parameters for the ionic conductivity in each linear region using the Arrhenius equation.

Region[a]	Phase III	Phase I[b]	Phase I[c]	Melt
T/ ℃	65−75	100−155	165−180	185−200
E_a/kJ mol^{-1}	228.3±27.5	36.7±1.3	403.7±20.2	31.0±2.7
σ_0/S cm^{-1}	6.41×10^{25}	0.0359	3.97×10^{42}	59.6
R^2 [d]	0.9715	0.9858	0.9925	0.9774

[a] Insufficient data for phase II. [b] Lower plateau region. [c] Steep region. [d] R^2: correlation coefficient.

(ii) Phase II

After the first solid-solid phase transition at 76.8 ℃, the ionic conductivity exceeds 1×10^{-8} S cm^{-1} in phase II, corresponding to the observed change of crystalline structure of **1** with the ions becoming disordered (Fig. 4). Additionally, the relatively fast increase of ionic conductivity in the temperature range 75−100 ℃ is accompanied by the observed plastic deformation between 80.8 and 100 ℃ (Fig. 5). Higher ionic conductivities in more disordered phases are considered to be associated with the ionic axial rotation and self-diffusion (at elevated temperatures).[55]

(iii) Lower plateau region (Phase I, 100−155 ℃)

After the second solid-solid phase transition at 87.2 ℃, the ionic conductivity of **1** gradually and nonlinearly rises to 2.58×10^{-7} S cm^{-1} at 100 ℃ and then comes to a lower plateau region over the temperature range of 100−155 ℃ resulting in a less notably increased ionic conductivity of 1.27×10^{-6} S cm^{-1} at 155 ℃. Overall, its ionic conductivity is superior to that of dried poly(4-styrenesulfonic acid) membrane (Fig. 11).[56a] Interestingly, **1** exhibits conductivity around two orders of magnitude higher than β-alumina-based ceramic proton conductors.[56b] It is about four or five orders of magnitude lower than that of pure imidazolium methanesulfonate (a POIPC) in its plastic phase[23] and fully hydrated Nafion.[56b] However, imidazolium methanesulfonate has a very narrow plastic phase region[23] and the proton conductivity of Nafion relies heavily on humidity.[56b,57] Compared with CsHSO$_4$, **1** displays a higher conductivity in the temperature range of 87−145 ℃ while CsHSO$_4$ shows a narrower temperature range of 144−212 ℃ for its plastic phase (superprotonic phase)[56c] and was reported to be unstable in fuel cell environments.[56d] In addition, between 170−180 ℃ the anhydrous ionic conductivity of **1** is about two or three orders of magnitude higher than that of CsH$_2$PO$_4$ measured under humidified air with a constant water content of 12 mol% (*i.e.* P(H$_2$O) = 0.12 atm).[56e] Although CsH$_2$PO$_4$ can reach a high ionic conductivity of around 1×10^{-2} S cm^{-1} at 250 ℃,[56e] it requires humidification for stabilization.[9,56e]

The direct current (DC) protonic conductivities (Fig. 11 and Table S1†) calculated from the slopes of the polarization curves at 120−160 ℃ (Fig. 14a) using Ohm's law agree very well with the corresponding AC ionic conductivities, suggesting that the measured ionic conductivity is primarily protonic in this region. This may be partially due to the fact that the anion is relatively large and long, thus its mobility in the lower plateau region is not significant. Furthermore, as the logarithm of the ionic conductivity in this region varies almost linearly with temperature (Fig. 12), the temperature dependence of ionic conductivity shows Arrhenius behavior. Particularly, in the lower plateau region E_a is estimated to be 36.7 ±1.3 kJ mol^{-1} (*i.e.* around 0.38 eV), which is about one sixth of the value for the low temperature ordered crystalline region (phase III) and is significantly low in

comparison with that for the dry Nafion® membrane (79 kJ mol^{-1}).[57] While the Grotthuss and the vehicle mechanisms have been proposed to interpret the proton conduction in solid compounds,[56b,58] the reported activation energies obtained through AC impedance data for the Grotthuss and the vehicle mechanisms are in the ranges of $0.1-0.4$ and $0.5-0.9$ eV, respectively.[8,55,56b,59] In detail, as hydrogen-bond cleavage requires an energy penalty in the range of 8.4–12.6 kJ mol^{-1} (0.087–0.13 eV),[59b,59c] proton conduction processes via Grotthuss mechanism thus generally involve $E_a < 0.4$ eV. With the vehicle mechanism, transport of larger ionic species (with greater mass compared to H$^+$) requires a larger energy contribution, and as such processes with $E_a > 0.4$ eV generally refers to the latter mechanism.[59b] Therefore, the rather low E_a in the lower plateau region leads us to assume that the underlying conduction mechanism is of the Grotthuss fashion (proton-hopping mechanism).[12,56b,59] In fact, the variable-temperature FT-IR spectra of **1** from 82 ℃ to 160 ℃ (Fig. S13a and S13b†) show that the N−H stretching region (3400−2600 cm^{-1}) as well as the single peak at 1558 cm^{-1} attributed to the protonation of 1H-1,2,4-triazole diminishes continuously, indicating the decreasing strength (hence longer length) of the N−H bonds. This is in contrast to the observation of increasing strength of N−H bonds with increasing temperature in protic ionic liquids.[29] The lengthened N−H bonds may favor the intermolecular proton transfer between neighbouring 1,2,4-triazolium cations. Likely, proton conduction occurs through a collective series of rotations by hydrogen-bonded cations with the −SO$_3^-$ groups of the anions acting possibly as "proton mediator".[61]

Furthermore, from 82 ℃ to 160 ℃ the SO$_3$ asymmetric stretching region weakens at the beginning (82−120 ℃) and then strengthens later (140−160 ℃) while the SO$_3$ symmetric stretching region and other vibrational bands associated with the anions constantly diminishes (Fig. S13a and S13b†). This, together with the weakening of N−H bonds, reflects a temperature sensitive and dynamic N−H⋯O hydrogen bonding network. It may confirm that the −SO$_3^-$ groups of the anions contribute to the increasing ionic conductivity likely via the role of "proton mediator". However, to fully clarify the proton conducting mechanism, proton diffusion coefficient measurements by ^{1}H-diffusion NMR, *e.g. pulsed magnetic field gradient spin echo NMR technique* (PGSE- or PFG-NMR), will be needed in the future research.[31b,58,60,63a]

(iv) Steep region (Phase I, 165−180 °C).

Further increase of the temperature after the lower plateau region in phase I leads to a rapid and linear increase of the conductivity from 2.62×10^{-6} S cm^{-1} at 165 ℃ to a liquid-like value of 1.07×10^{-4} S cm^{-1} at 180 ℃ shortly before melting, indicating the greatly increased disorder of **1** in this steep region. The ionic conductivity is so temperature-dependent that the E_a is estimated to be as high as 403.7 ± 20.2 kJ mol^{-1}, which is more than 10 times of estimated E_a (36.7 ± 1.3 kJ mol^{-1}) in the lower plateau region (100−155 ℃) (Table 4). Upon heating to 165 ℃, the infrared bands firstly grow stronger but soon diminish quickly (Fig. S13c†) while a movie (Movie S1†) for another crystal of **1** demonstrates the thermal-induced plastic flow when the crystal was heated at 165 ℃ for ~3 min. The plastic flow is also confirmed by the microscopic images taken during the variable temperature FT-IR measurements, which show no fundamental

morphological changes from 60 to 160 ℃ (Fig. S16†) but thorough transformation after reaching 165 ℃ for a few minutes (Fig. S17†). The plastic flow at 165 ℃, which may be regarded as a "qualitative change" compared with the observed thermal-induced, slow plastic deformation from 82 to 118 ℃ (Fig. 6b and 6c), should be correlated with the strong temperature-dependence of ionic conductivity at temperatures $\geq$ 165 ℃. Furthermore, **1** almost loses its crystallinity at 165 ℃ and becomes amorphous at temperatures $\geq$ 170 ℃ prior to melting as revealed by the nearly complete disappearance of sharp X-ray diffraction peaks (Fig. S18†). Visual observation confirms that bulk samples of **1** are still solid below 181 ℃. This is similar to what we observed for imidazolium methanesulfonate, whose crystallinity was lost at around 184 ℃ prior to its melting transition at 188 ℃.[23]

The mechanism of the rapid increase of ionic conductivity and the observed plastic flow are believed to be connected with the dynamics of both the anions and the cations. Previously, organic ions such as tetrabutylammonium and di-n-alkylammonium cations have been discovered to be able to diffuse in the plastic crystalline phases.[35,55] It has also been reported that both the cation and the anion of diethyl(methyl)(isobutyl)phosphonium hexafluorophosphate ([P$_{1,2,2,4}$][PF$_6$]) can diffuse in its plastic phase.[16] Interestingly, the greatly increased E_a for **1** from the lower plateau region (100−155 ℃) to the steep region (165−180 °C) is analogous to the rotator phase revealed in di-n-alkylammonium bromides where cations perform axial reorientation around the molecular axis with a low E_a and translational self-diffusion at elevated temperatures involving a much higher E_a.[55] It is thus speculated that at least the cation and probably both the cation and the anion can diffuse in the steep region (phase I, 165−180 °C). This is supported by the facts that **1** begins to lose its crystallinity from 165 ℃ and exhibits a plastic flow coupled with a relatively high ionic conductivity. Hence, the observed high ionic conductivity may arise from not only the intermolecular proton transfer (proton-hopping), but also the onset of the diffusion of 1,2,4-triazolium cations (vehicle mechanism).[62] Furthermore, at 170 ℃ and 180 ℃ the calculated direct-current (DC) protonic conductivity is evidently lower than the measured AC ionic conductivity (Fig. 11), suggesting that the anions contribute to the ionic conduction significantly in the steep region. In fact, upon heating from 160 ℃ to 180 ℃, the material undergoes significant structural changes as revealed by the alteration of strength of the N−H stretching and the SO$_3$ asymmetric stretching vibrational bands (Fig. S13c, S13d, S13e and S13f†), indicating the consequent dynamics of the anions and the cations.

(v) Molten state.

The phase I → melt transition enables an increase in the ionic conductivity by two orders of magnitude higher, reaching 1.74×10^{-2} S cm^{-1} at 185 ℃. The conductivity in the molten state rises steadily with E_a of 31.0 ± 2.7 kJ mol^{-1} and ultimately reaches a value as high as 2.23×10^{-2} S cm^{-1} at 200 ℃. Similar to some other protic ionic liquids,[63] the vehicle mechanism[62] may be postulated to govern the proton conduction for **1** in the molten state with the 1,2,4-triazolium cation as a vehicle.

Electrochemical hydrogen pumping

During the hydrogen pumping tests at 150 ^{o}C, a stable current density of about 30.6 μA cm^{-2} was observed after about 150 s

under a DC voltage of 1.0 V (Fig. 13). This current is assumed to correspond to the hydrogen pumping process, *i.e.* hydrogen oxidation at the anode and meanwhile hydrogen evolution at the cathode. When the cell voltage was set to 0.50 V, the obtained constant current density was about 14.3 μA cm^{-2}. This nearly ohmic/linear behavior is expected as the hydrogen oxidation and evolution on platinum catalysts are electrochemically reversible with little overpotential in this current range. During the chronoamperometric measurement at 0.50 V, when the hydrogen flow was switched to argon for both sides, the current density immediately attenuated to zero (Fig. 13). After about 130 s, the hydrogen flow was restored and so was the constant current. It shows clearly that the observed ionic conductivity is of protonic nature, with the following processes occurring dominantly in the hydrogen pumping cell:

Anode: $H_2 \rightarrow 2H^+ + 2e^-$
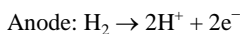
Electrolyte (**1**): H^+ conducts from anode to cathode

Cathode: $2H^+ + 2e^- \rightarrow H_2$

In addition, as the cell was operating with dry gas (without humidifcation), no other proton carriers such as water molecules were present. Therefore, the observed constant current (Fig. 13) also hints steady proton conduction with little help of vehicular carriers, further excluding conduction of any species except protons and suggesting proton conduction via Grotthuss mechanism (proton-hopping) at 150 ℃ in the lower plateau region (Phase I, 100−155 ℃) (Fig. 12).
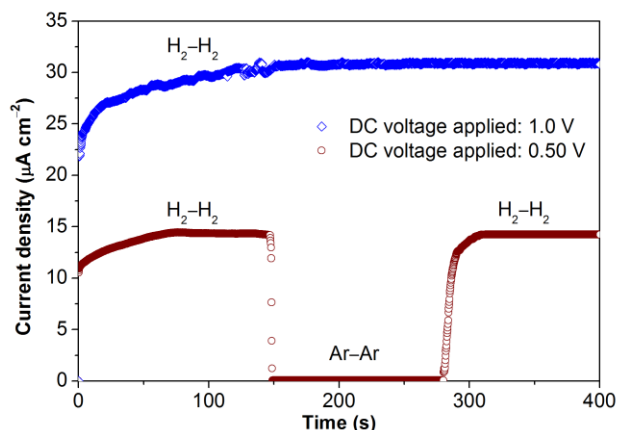
Fig. 13 Chronoamperometric curves of a hydrogen pumping cell consisting of a 0.5 mm thick pellet electrolyte and two platinum gas diffusion electrodes under a DC voltage of 1.0 V and 0.50 V, respectively. The cell was supplied with a dry hydrogen flow on both sides, which was for a period switched to dry argon when the applied DC voltage was 0.50 V as indicated in the figure.

Fuel cell performance

To further obtain the direct evidence of long-range proton conduction,[12] a cylindrical dense pellet of **1** was used as the electrolyte and assembled with electrodes made from Pt/C catalysts on each side to form a single fuel cell. The electromotive force of the dry hydrogen/air fuel cell and the polarization curves were measured from 120 ℃ to 180 ℃, a temperature range typical for high temperature PEMFCs. Fig. 14a presents the polarization curves recorded by linear sweep voltammetry at a scan rate of 10 mV s^{-1}, indicating that the conducting species are protons coupled with facile hydrogen oxidation and oxygen reduction under non-humidified conditions in the anode and the cathode, respectively.
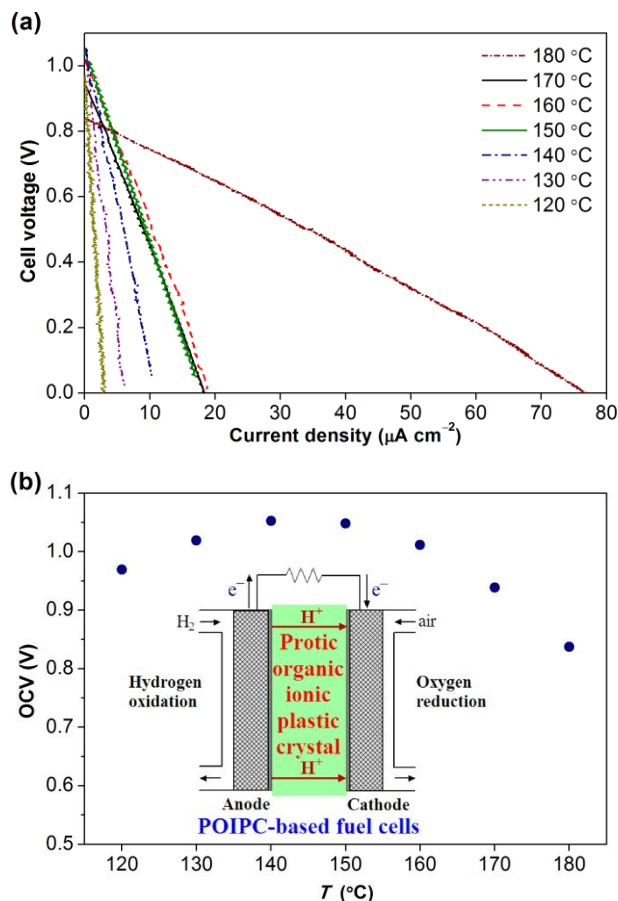

Fig. 14 (a) Polarization curves and (b) the corresponding open circuit voltages measured at different temperatures, using the following electrochemical cell: H$_2$ (1 atm), Pt/C|cylindrical dense pellet of **1**|Pt/C, dry air (1 atm). The pellet had a diameter of 13 mm and a thickness of 1.0 mm. It was assembled with Pt/C electrodes (contact surface area: 0.50 cm^2) on each side to form a single cell. Pt loading of each electrode was 7 mg Pt cm^{-2}. The polarization curves were recorded from 120 ℃ to 180 ℃ by linear sweep voltammetry at a scan rate of 10 mV s^{-1}. Inset: schematic of the proof-of-concept fuel cell based on POIPCs. Note that the cylindrical pellets used for the ionic conductivity measurements (Fig. 11) and fuel cell evaluations were prepared in the same way (only the thickness is slightly different).

Although the drop in cell voltage with increasing current density (Fig. 14a) has many causes,[1a,c] similar to the fuel cells with thick CsHSO$_4$ membranes,[8] for the 1.0 mm thick electrolyte of **1** as was used in this experiment, the primary cause is the resistance of the electrolyte, if one also takes the low conductivity of **1** into consideration (*e.g.* 1.19×10^{-6} S cm^{-1} at 150 ℃). As expected, the cell voltage drops linearly as a function of current density, the slope of which is equal to d/σ, where d is the thickness of the electrolyte and σ the conductivity (Table S1†). On the whole, the slopes of the polarization curves decrease with increasing temperature (Table S1†), suggesting the decreased cell

resistance, which is almost equal to the through-plane resistance of the cylindrical pellet of **1**. The calculated ionic conductivity (Fig. 11 and Table S1†) based on the slopes of the polarization curves may thus confirm the DC protonic conductivity of the cylindrical dense pellet of **1**.

Fig. 14b details the corresponding open circuit voltages (OCVs) shown in Fig. 14a. From 120 ℃ to 160 ℃, high OCVs are achieved. For example, the OCV reaches 1.05 V at 150 ℃ without humidity, approaching the theoretical maximum (1.11 V) at 150 ℃ and 1 atm pressure for the formation of water vapor from the hydrogen/air fuel cell.[64] This value is much higher than the reported OCVs for membrane-type fuel cells based on protic ionic liquids[4–7] and H_3PO_4 doped polybenzimidazole membranes.[2] This result further indicates that the conducting species are protons transported through hydrogen bond networks in the pellet of **1**, because oxide anions (O^{2-}) are unlikely to be generated or move in **1** in this temperature range, and no other ions can generate an OCV in this membrane-electrode assembly (MEA).[11,12] The high OCV may be partially attributed to the low permeability of oxygen and hydrogen in even molten fluoroalkylsulfonates,[65,66] inhibiting the crossover of oxygen and hydrogen through the solid and dense electrolyte film of **1** in the fuel cell.

Furthermore, the high OCV value can be correlated with ΔpK_a, which denotes the difference in aqueous solution pK_a values for the constituent base and acid of the protic salt. As n-$C_4F_9SO_3H$ has very close acidity with another super acid CF_3SO_3H,[67] its pK_a value can be estimated to be the same with that of CF_3SO_3H (pK_a = −13).[68] Since the reported pK_a value of $1H$-1,2,4-triazole is 2.27,[69] ΔpK_a of protic salt **1** is estimated to be 15.27, suggesting the complete proton transfer from n-$C_4F_9SO_3H$ to $1H$-1,2,4-triazole (ΔpK_a > 10).[70] According to $\Delta G_{(proton\ transfer)}$ = −2.303R$T\Delta pK_a$ proposed by Angell *et al.*,[71] the proton energy gap between the donor acid and the acceptor base of the protic salt **1** is 0.90 eV at 25 ℃, falling in the range of proton energy gap of 0.6−1.0 eV for protic ionic liquids with extremely high OCVs for liquid-electrolyte-based fuel cells.[71]

Further increase of the temperature to 170 ℃ and 180 ℃ leads to a decreased OCV of 0.938 V and 0.837 V, respectively. The drop of OCVs may be attributed to the plastic flow (Movie S1†) and the simultaneous transformation from plastic crystalline into plastic amorphous state (Fig. S18†), which happens at temperatures ≥ 165 ℃ and may allow fuel crossover, indicating that POIPCs should be sufficiently flexible to adapt to changes in morphology of electrodes and meantime avoid excessive plastic flow.

Nevertheless, the wide plastic phase (87 ℃ − 181 ℃) of **1** clearly matches well the typical working temperature range of high temperature PEMFCs. Furthermore, the almost constant, high OCV profile of a pressed pellet of as-synthesized powders of **1** at 25 ℃ over 4000 s demonstrates the stability of the material in the dry hydrogen/air fuel cell environments (Fig. S19†).

Finally, while the moisture absorbing property is intrinsic for phosphoric acid absorbed membranes, which are the current benchmark high temperature PEMFC electrolytes,[2] our POIPC electrolyte is not hygroscopic (though water soluble) without detectable moisture absorbing property after its exposure in nearly fully humid air for 48 h at room temperature (see Supporting Information†).

All in all, our results show that POIPCs are promising for the realization of all-solid-state high temperature PEMFCs. Further work on (*i*) **1** and other POIPCs with wider temperature ranges of plastic phases and better electrochemical properties as proton conductors for fuel cells, and (*ii*) evaluation of high temperature PEMFC performance of polymer electrolyte membranes based on POIPCs are in progress in our labs.

Conclusions

Protic organic ionic plastic crystals (POIPCs) represent an exciting novel class of solid state proton conductors for fuel cells, particularly high temperature PEMFCs. With 1,2,4-triazolium perfluorobutanesulfonate (**1**) as an archetypal example with a wide temperature range of plastic phase, they exhibit unique material properties and provide a competitive alternative to current proton conductors based on aqueous systems, phosphoric acid, organic solvents, solid acids, or protic ionic liquids. Fundamentally, we have illustrated that the key property that distinguishes POIPCs from aprotic OIPCs is the proton transfer from the Brønsted acid to the Brønsted base, leading to the presence of proton-donor and proton-acceptor sites and the formation of a strong hydrogen bonding network. Consequently, hydrogen bonding plays a crucial role in the physicochemical properties of POIPCs and thus deserves further experimental and theoretical investigations. The ionic and solid nature of POIPCs offers the additional merit of non-flammability, negligible volatility, superior thermal stability and ease of handling while eliminating the problem of leakage associated with liquid electrolytes. In addition, their plasticity is expected to benefit the accommodation of thermal-induced volume changes in fuel cell applications. Hence they are desirable for all-solid-state fuel cells from the perspective of devices. The use of **1** as an anhydrous proton conductor for all-solid-state high temperature H_2/air fuel cells demonstrates the fuel cell polarization curves with ultra-high and constant open circuit voltages, indicating that POIPCs are promising for the realization of all-solid-state PEMFCs. Interestingly, similar to protic ionic liquids, the open circuit voltage for a POIPC seems to be correlated with the ΔpK_a value between the Brønsted base and the Brønsted acid. To the best of our knowledge, this is the first report of the proof of principle of a POIPC-based fuel cell. We hope that our work will stimulate further investigation of this novel group of proton conductors. Furthermore, we anticipate that POIPCs may also find applications in other electrochemical devices such as sensors and flexible supercapacitors.

Acknowledgements

single-crystal X-ray diffractometer (KU Leuven) through project AKUL/09/0035. We thank Mr. Danny Winant (KU Leuven) for the TGA, DSC and TMA measurements, Mr. Rudy De Vos (KU Leuven) for the SEM images, Dr Chang Chen and Mr. Sarp Kerman (IMEC) for the Raman tests, and Mr. Pieterjan Valvekens (KU Leuven) for adjusting the Varian 670-IR FT-IR spectrometer. J.L appreciates technical discussions with Prof. Dr Douglas R. MacFarlane (Monash University) and Dr Olaf Conrad (University of Cape Town).

Notes and references

a Department of Materials Engineering, KU Leuven, Leuven 3001, Belgium. Fax: +32 16 3 21990; Tel: +32 16 32 12 39; E-mail: jan.fransaer@mtm.kuleuven.be

b Centre for Surface Chemistry and Catalysis, KU Leuven, Leuven 3001, Belgium. Fax: +32 16 3 21998; E-mail: dirk.devos@biw.kuleuven.be; jiangshui.luo@biw.kuleuven.be;

c Department of Energy Conversion and Storage, Technical University of Denmark, Kgs. Lyngby 2800, Denmark. Fax: +45 45 88 31 36; Tel: +45 45 25 23 18; E-mail: qfli@dtu.dk

d Department of Chemistry, KU Leuven, Leuven 3001, Belgium. Fax: +32 16 3 27992; Tel: +32 16 32 74 46; E-mail: koen.binnemans@chem.kuleuven.be

e Department of Physics, University of Oldenburg, Oldenburg 26129, Germany.

f Department of Physics and Astronomy, KU Leuven, Leuven 3001, Belgium.

g Department of Polymer Science and Engineering, Soochow University, Suzhou 215123, China.

h Dalian Institute of Chemical Physics, Chinese Academy of Sciences, Dalian 116023, China.

i School of Chemistry and Chemical Engineering, Shanghai Jiao Tong University, Shanghai 200240, China.

† Electronic Supplementary Information (ESI) available: [Supplementary experiments; supplementary analysis; supplementary figures including infrared analysis, thermogravimetric analysis, polarized optical microscopic images, DSC curves, powder XRD patterns, crystal data, Raman spectra, images of the crystal recorded during variable-temperature FT-IR measurements, and OCV at 25 °C versus time; a supplementary table showing the fitting slopes of the polarization curves. A supplementary movie showing the plastic flow of a crystal at $t = \sim3$ min when it was heated at 165 °C. Crystallographic information files (CIF) for the crystal structures determined at 100 K and 300 K, respectively. CCDC reference numbers 1013012−1013013.]. See DOI: 10.1039/b000000x/

‡ Dedicated to Professor Baolian Yi.

1   (*a*) B. Yi, *Fuel Cells—Principle, Technology and Application*, Chemical Industry Press, Beijing, 2003; (*b*) H. A. Gasteiger and N. M. Marković, *Science*, 2009, **324**, 48; (*c*) M. K. Debe, *Nature*, 2012, **486**, 43.

2   (*a*) Q. Li, J. O. Jensen, R. F. Savinell and N. J. Bjerrum, *Prog. Polymer Sci.*, 2009, **34**, 449; (*b*) J. S. Wainright, J.-T. Wang, D. Weng, R. F. Savinell and M. Litt, *J. Electrochem. Soc.*, 1995, **142**, L121.

3   (*a*) M. Armand, F. Endres, D. R. MacFarlane, H. Ohno and B. Scrosati, *Nat. Mater.*, 2009, **8**, 621; (*b*) M. Díaz, A. Ortiz and I. Ortiz, *J. Membr. Sci.*, 2014, **469**, 379.

4   J. S. Lee, T. Nohira and R. Hagiwara, *J. Power Sources*, 2007, **171**, 535.

5   S.-Y. Lee, A. Ogawa, M. Kanno, H. Nakamoto, T. Yasuda and M. Watanabe, *J. Am. Chem. Soc.*, 2010, **132**, 9764.

6   T. Yasuda, S. Nakamura, S. Y. Lee and M. Watanabe, *Chem. Lett.*, 2010, **39**, 678.

7   C. Ke, J. Li, X. Li, Z. Shao and B. Yi, *RSC Advances*, 2012, **2**, 8953.

8   S. M. Haile, D. A. Boysen, C. R. I. Chisholm and R. B. Merle, *Nature*, 2001, **410**, 910

9   D. A. Boysen, T. Uda, C. R. I. Chisholm and S. M. Haile, *Science*, 2004, **303**, 68.

10 J. A. Hurd, R. Vaidhyanathan, V. Thangadurai, C. I. Ratcliffe, I. L. Moudrakovski and G. K. H. Shimizu, *Nature Chem.*, 2009, **1**, 705.

11 S. Horike, D. Umeyama, M. Inukai, T. Itakura and S. Kitagawa, *J. Am. Chem. Soc.*, 2012, **134**, 7612.

12 D. Umeyama, S. Horike, M. Inukai, T. Itakura and S. Kitagawa, *J. Am. Chem. Soc.*, 2012, **134**, 12780.

13 J. Luo, Ph.D. Thesis, KU Leuven, 2012.

14 D. R. MacFarlane and M. Forsyth, *Adv. Mater.*, 2001, **13**, 957.

15 J. M. Pringle, *Phys. Chem. Chem. Phys.*, 2013, **15**, 1339.

16 L. Jin, K. M. Nairn, C. M. Forsyth, A. J. Seeber, D. R. MacFarlane, P. C. Howlett, M. Forsyth and J. M. Pringle, *J. Am. Chem. Soc.*, 2012, **134**, 9688.

17 J. Timmermans, *J. Phys. Chem. Solids*, 1961, **18**, 1.

18 (*a*) D. R. MacFarlane, J. H. Huang and M. Forsyth, *Nature*, 1999, **402**, 792; (*b*) L. Jin, P. C. Howlett, J. M. Pringle, J. Janikowski, M. Armand, D. R. MacFarlane and M. Forsyth, *Energy Environ. Sci.*, 2014, **7**, 3352.

19 (*a*) S. Li, L. Qiu, C. Shi, X. Chen and F. Yan, *Adv. Mater.*, 2014, **26**, 1266; (*b*) V. Armel, M. Forsyth, D, R. MacFarlane and J. M. Pringle, *Energy Environ. Sci.*, 2011, **4**, 2234.

20 Y. Abu-Lebdeh, A. Abouimrane, P.-J. Alarco, A. Hammami, L. Ionescu-Vasii and M. Armand, *Electrochem. Commun.*, 2004, **6**, 432.

21 S. Long, P. C. Howlett, D. R. MacFarlane and M. Forsyth, *Solid State Ionics*, 2006, **177**, 647.

22 U. A. Rana, R. Vijayaraghavan, D. R. MacFarlane and M. Forsyth, *Chem. Commun.*, 2011, **47**, 6401.

23 J. Luo, O. Conrad and I. F. J. Vankelecom, *J. Mater. Chem. A*, 2013, **1**, 2238.

24 H. Suga, M. Sugisaki and S. Seki, *Mol. Cryst.*, 1966, **1**, 377.

25 (*a*) K. Kuchitsu, H. Ono, S. Ishimaru, R. Ikeda and H. Ishida, *Phys. Chem. Chem. Phys.*, 2000, **2**, 3883; (*b*) P. Szklarz, A. Pietraszko, R. Jakubas, G. Bator, P. Zieliński and M. Gałazka, *J. Phys.: Condens. Matter*, 2008, **20**, 255221.

26 (*a*) G. M. Sheldrick, *Acta Crystallogr., Sect. A: Found. Crystallogr.*, 2008, **64**, 112; (*b*) O. V. Dolomanov, L. J. Bourhis, R. J. Gildea, J. A. K. Howard and H. Puschmann, *J. Appl. Crystallogr.*, 2009, **42**, 339.

27 (*a*) J. Luo, J. Hu, W. Saak, R. Beckhaus, G. Wittstock, I. F. J. Vankelecom, C. Agert and O. Conrad, *J. Mater. Chem.*, 2011, **21**, 10426; (*b*) J. Luo, O. Conrad and I. F. J. Vankelecom, *J. Mater. Chem.*, 2012, **22**, 20574.

28 E. S. Stoyanov, K. C. Kim and C. A. Reed, *J. Am. Chem. Soc.*, 2006, **128**, 8500.

29 M. S. Miran, H. Kinoshita, T. Yasuda, M. A. B. H. Susana and M. Watanabe, *Chem. Commun.*, 2011, **47**, 12676.

30 D. Bougeard, N. Le Calvé, B. Saint Roch and A. Novak, *J. Chem. Phys.*, 1976, **64**, 5152.

31 (*a*) K. D. Kreuer, A. Fuchs, M. Ise, M. Spaeth and J. Maier, *Electrochim. Acta*, 1998, **43**, 1281; (*b*) S. Li, Z. Zhou, Y. Zhang, M. Liu and W. Li, *Chem. Mater.*, 2005, **17**, 5884.

32 Y. Huang, Q. Li, A. H. Jensen, M. Yin, J. O. Jensen, E. Christensen, C. Pan, N. J. Bjerrum and W. Xing, *J. Mater. Chem.*, 2012, **22**, 22452.

33 S. A. Forsyth, K. J. Fraser, P. C. Howlett, D. R. MacFarlane and M. Forsyth, *Green Chem.*, 2006, **8**, 256.

34 J. Sun, D. R. MacFarlane and M. Forsyth, *Solid State Ionics*, 2002, **148**, 145.

35 R. Asayama, J. Kawamura and T. Hattori, *Chem. Phys. Lett.*, 2005, **414**, 87.

36 T. Enomoto, S. Kanematsu, K. Tsunashima, K. Matsumoto and R. Hagiwara, *Phys. Chem. Chem. Phys.*, 2011, **13**, 12536.

37 W. A. Henderson, D. M. Seo, Q. Zhou, P. D. Boyle, J.-H. Shin, H. C. De Long, P. C. Trulove and S. Passerini, *Adv. Energy Mater.*, 2012, **2**, 1343.

38 V. Armel, D. Velayutham, J. Sun, P. C. Howlett, M. Forsyth, D. R. MacFarlane and J. M. Pringle, *J. Mater. Chem.*, 2011, **21**, 7640.

39 A. Torrisi, C. K. Leech, K. Shankland, W. I. F. David, R. M. Ibberson, J. Benet-Buchholz, R. Boese, M. Leslie, C. R. A. Catlow and S. L. Price, *J. Phys. Chem. B*, 2008, **112**, 3746.

40 J. N. Sherwood, *Plastically Crystalline State: Orientationally Disordered Crystals*, John Wiley & Sons, New York, 1979.

41 G. Annat, J. Adebahr, I. R. McKinnon, D. R. MacFarlane and M. Forsyth, *Solid State Ionics*, 2007, **178**, 1065.

42 S. J. Pas, J. M. Pringle, M. Forsyth and D. R. MacFarlane, *Phys. Chem. Chem. Phys.*, 2004, **6**, 3721.

43 Y. Shekibi, T. Ruether, J. Huang and A. F. Hollenkamp, *Phys. Chem. Chem. Phys.*, 2012, **14**, 4597.

44 A. J. Hill, J. Huang, J. Efthimiadis, P. Meakin, M. Forsyth and D. R. MacFarlane, *Solid State Ionics*, 2002, **154−155**, 119.

45 J. Efthimiadis, S. J Pas, M. Forsyth and D. R. MacFarlane, *Solid State Ionics*, 2002, **154−155**, 279.

46 (*a*) M. A. Harmer, C. P. Junk, V. V. Rostovtsev, W. J. Marshall, L. M. Grieco, J. Vickery, R. Miller and S. Work, *Green Chem.*, 2009, **11**, 517; (*b*) I. Brüdgam, D. Lentz and H. Vorbrüggen, *CrystEngComm*, 2010, **12**, 795.

47 R. Qiu, S. Yin, X. Song, Z. Meng, Y. Qiu, N. Tan, X. Xu, S. Luo, F.-R. Dai, C.-T. Au and W.-Y. Wong, *Dalton Trans.*, 2011, **40**, 9482.

48 K. Fumino, A. Wulf and R. Ludwig, *Angew. Chem. Int. Ed.*, 2009, **48**, 3184.

49 K. Fumino, E. Reichert, K. Wittler, R. Hempelmann and R. Ludwig, *Angew. Chem. Int. Ed.*, 2012, **51**, 6236.

50 P. Kölle and R. Dronskowski, *Inorg. Chem.*, 2004, **43**, 2803.

51 S. M. Chackalackal and F. E. Stafford, *J. Am. Chem. Soc.*, 1966, **88**, 4815.

52 C. P Lawrence and J. L Skinner, *Chem. Phys. Lett.*, 2003, **369**, 472.

53 H.-S. Tan, I. R. Piletic, R. E. Riter, N. E. Levinger and M. D. Fayer, *Phys. Rev. Lett.*, 2005, **94**, 057405.

54 N. A. Murugan, *J. Phys. Chem. B*, 2005, **109**, 23955.

55 T. Shimizu, S. Tanaka, N. Onoda-Yamamuro, S. Ishimaru and R. Ikeda, *J. Chem. Soc., Faraday Trans.*, 1997, **93**, 321.

56 (*a*) T. Okayasu, K. Hirose and H. Nishide, *Polym. Adv. Technol.*, 2011, **22**, 1229; (*b*) K.-D. Kreuer, *Chem. Mater.*, 1996, **8**, 610; (*c*) D. A. Boysen, C. R. I. Chisholm, S. M. Haile and S. R. Narayanan, *J. Electrochem. Soc.*, 2000, **147**, 3610; (*d*) R. B. Merle, C. R. I. Chisholm, D. A. Boysen and S. M. Haile, *Energy & Fuels*, 2003, **17**, 210; (*e*) A. H. Jensen, Q. Li, E. Christensen and N. J. Bjerrum, *J. Electrochem. Soc.*, 2014, **161**, F72.

57 T. Tago, H. Shibata and H. Nishide, *Chem. Commun.*, 2007, 2989.

58 (*a*) P. Colomban, *Proton Conductors: Solids, Membranes and Gels—Materials and Devices*, Cambridge University Press, Cambridge, 1992; (*b*) G. Scharfenberger, W. H. Meyer, G. Wegner, M. Schuster, K.-D. Kreuer and J. Maier, *Fuel Cells*, 2006, **6**, 237; (*c*) J. W. Traer, K. J. Soo, M. Vijayakumar and G. R. Goward, *J. Phys. Chem. C*, 2011, **115**, 6064.

59 (*a*) A. Shigematsu, T. Yamada and H. Kitagawa, *J. Am. Chem. Soc.*, 2011, **133**, 2034; (*b*) P. Ramaswamy, N. E. Wong and G. K. H. Shimizu, *Chem. Soc. Rev.*, 2014, **43**, 5913; (*c*) N. Agmon, *Chem. Phys. Lett.*, 1995, **244**, 456.

60 (*a*) D. W. McCall, D. C. Douglass and E. W. Anderson, *Ber. Bunsenges. Phys. Chem.*, 1963, **67**, 366; (*b*) E. O. Stejskal and J. E. Tanner, *J. Chem. Phys.*, 1965, **42**, 288; (*c*) J. E. Tanner, *J. Chem. Phys.*, 1970, **52**, 2523; (*d*) Th. Dippel, K. D. Kreuer, J. C. Lassègues and D. Rodriguez, *Solid State Ionics*, 1993, **61**, 41; (*e*) A. Noda, K. Hayamizu and M. Watanabe, *J. Phys. Chem. B*, 2001, **105**, 4603; (*f*) R. Taniki, K. Matsumoto, R. Hagiwara, K. Hachiya, T. Morinaga and T. Sato, *J. Phys. Chem. B*, 2013, **117**, 955; (*g*) K. Romanenko, L. Jin, L. A. Madsen, J. M. Pringle, L. A. O'Dell and M. Forsyth, *J. Am. Chem. Soc.*, 2014, **136**, 15638.

61 S. Y. Kim, S. Kim and M. J. Park, *Nat. Commun.*, 2010, **1**, 88.

62 K.-D. Kreuer, A. Rabenau and W. Weppner, *Angew. Chem. Int. Ed. Engl.*, 1982, **21**, 208.

63 (*a*) H. Nakamoto and M. Watanabe, *Chem. Commun.*, 2007, 2539; (*b*) J. Luo, T. V. Tan, O. Conrad and I. F. J. Vankelecom, *Phys. Chem. Chem. Phys.*, 2012, **14**, 11441.

64 J. Zhang, Y. Tang, C. Song, J. Zhang and H. Wang, *J. Power Sources*, 2006, **163**, 532.

65 M. Haibara, S. Hashizume, H. Munakata and K. Kanamura, *Electrochim. Acta*, 2014, **132**, 208.

66 S. Mitsushima, Y. Shinohara, K. Matsuzawa and K. Ota, *Electrochim. Acta*, 2010, **55**, 6639.

67 A. G. Posternak, R. Y. Garlyauskayte, V. V. Polovinko, L. M. Yagupolskii and Y. L. Yagupolskii, *Org. Biomol. Chem.*, 2009, **7**, 1642.

68 D. R. MacFarlane, J. M. Pringle, K. M. Johansson, S. A. Forsyth and M. Forsyth, *Chem. Commun.*, 2006, 1905.

69 W. L. F. Armarego and C. L. L. Chai, *Purification of Laboratory Chemicals*, Butterworth-Heinemann, Oxford, 6th edn, 2009.

70 M. Yoshizawa, W. Xu and C. A. Angell, *J. Am. Chem. Soc.*, 2003, **125**, 15411.

71 J.-P. Belieres, D. Gervasio and C. A. Angell, *Chem. Commun.*, 2006, 4799.

Broader context

The ever-increasing need for efficient energy production and storage urges the development of electrolyte materials for electrochemical devices ranging from fuel cells and dye-sensitized solar cells for electricity generation to lithium-ion batteries and supercapacitors for energy storage. Among various electrolytes, proton conductors are crucial materials for polymer electrolyte membrane fuel cells (PEMFCs). In particular, high temperature PEMFCs, which work in the temperature range of 100−200 °C, are more beneficial than the widespread PEMFCs based on hydrated Nafion® membranes. However, the state-of-the-art high temperature PEMFCs involve liquid electrolytes (*e.g.* H_3PO_4), and thus suffer from leakage and long-term instability. Consequently, suitable solid-state proton conductors are urgently needed for the development of practical high temperature PEMFCs. Here, with 1,2,4-triazolium perfluorobutanesulfonate as an archetypal example, it is demonstrated as "proof of principle" that protic organic ionic plastic crystals (POIPCs) with a wide plastic crystalline phase are a type of new, promising anhydrous solid-state proton conductors for all-solid-state fuel cells. It is anticipated that POIPCs may also find applications in other electrochemical devices (*e.g.* sensors).

Electronic Supplementary Information

1,2,4-Triazolium perfluorobutanesulfonate as an archetypal pure protic organic ionic plastic crystal electrolyte for all-solid-state fuel cells

Jiangshui Luo,*[a,b] Annemette H. Jensen,[c] Neil R. Brooks,[d] Jeroen Sniekers,[d] Martin Knipper,[e] David Aili,[c] Qingfeng Li,*[c] Bram Vanroy,[f] Michael Wübbenhorst,[f] Feng Yan,[g] Luc Van Meervelt,[d] Zhigang Shao,[h] Jianhua Fang,[i] Zheng-Hong Luo,[i] Dirk E. De Vos,*[b] Koen Binnemans*[d] and Jan Fransaer*[a]

[a] Department of Materials Engineering, KU Leuven, Leuven 3001, Belgium. Fax: +32 16 3 21990; Tel: +32 16 32 12 39; E-mail: jan.fransaer@mtm.kuleuven.be
[b] Centre for Surface Chemistry and Catalysis, KU Leuven, Leuven 3001, Belgium. Fax: +32 16 3 21998; E-mail: dirk.devos@biw.kuleuven.be; jiangshui.luo@biw.kuleuven.be;
[c] Department of Energy Conversion and Storage, Technical University of Denmark, Kgs. Lyngby 2800, Denmark. Fax: +45 45 88 31 36; Tel: +45 45 25 23 18; E-mail: qfli@dtu.dk
[d] Department of Chemistry, KU Leuven, Leuven 3001, Belgium. Fax: +32 16 3 27992; Tel: +32 16 32 74 46; E-mail: koen.binnemans@chem.kuleuven.be
[e] Department of Physics, University of Oldenburg, Oldenburg 26129, Germany.
[f] Department of Physics and Astronomy, KU Leuven, Leuven 3001, Belgium.
[g] Department of Polymer Science and Engineering, Soochow University, Suzhou 215123, China.
[h] Dalian Institute of Chemical Physics, Chinese Academy of Sciences, Dalian 116023, China.
[i] School of Chemistry and Chemical Engineering, Shanghai Jiao Tong University, Shanghai 200240, China.

Table of Contents

*Section 4***:** *Supplementary Table*

*Section 5***:** *Supplementary Movie*

2

Section 1: Supplementary Experiments

NMR analysis

^{1}H NMR (400 MHz, DMSO-d_6): δ 9.33 (s, 2H, C−H), δ 14.3 (s, 2H, N−H). ^{13}C NMR (100 MHz, DMSO-d_6): δ 143.16, δ 39.39.

Temperature-dependent powder XRD patterns for a pressed cylindrical dense pellet:

Temperature-dependent powder XRD patterns for a pressed cylindrical dense pellet of **1** was recorded in an argon atmosphere from 25 ℃ to 160 ℃ on a powder X-ray diffractometer (X'Pert PRO, PANalytical) using Cu Kα radiation ($\lambda = 1.5406$ Å). The cylindrical dense pellet was prepared by uniaxial pressing of fine powders of **1** in a 10 mm diameter metal die under 20 kN (corresponding to a pressure of 255 MPa) for 1 min. Measurements were done in a high-temperature oven chamber (HTK 1200N, Anton Paar) using a coin-like metal sample holder. The heating element installed is a Kanthal APM (Cr: 22%; Al: 5.8%; Fe: rest) and the thermocouple is a Pt-10%Rh-Pt sensor (type S). The sample was stabilized at each measurement temperature (accuracy: ±1 ℃) for about 20 min before each measurement. The temperature ramp between two consecutive temperatures was 2 ℃ min^{-1}. Each measurement consisted of a $\theta-2\theta$ scan from 10° to 50° with a step size of 0.052° and a scan speed of 0.039° s^{-1}.

Comparison of moisture absorbing property:

Certain amounts of **1** and 85% H_3PO_4 were weighed in dry and clean beakers and then placed on a dry plate in a closed pot with plenty of water filled at the bottom of the pot to compare the respective gain of weight at room temperature after 48 h. The air in the closed system could be considered nearly fully humid. It was found that **1** was not hygroscopic without detectable gain of weight (accuracy of the balance used: ±0.1 mg) while 85% H_3PO_4 showed obvious increase of weight ($\Delta m/m \times 100\%$ $= \frac{2.3344 \, \text{g}}{23.8365 \, \text{g}} \times 100\% = 9.79\%$) indicating its strong moisture absorbing property.

Section 2: Supplementary Infrared, Thermal and Structural Analysis

Infrared analysis

The absence of both of the O−H stretching bands between 3400 and 3800 cm^{-1} and the H−O−H bending band at around 1650 cm^{-1} in the FT-IR spectrum (Fig. S1) confirms the very low water content of **1**.[S1−S3] The ultra-low water content may also be further indicated by the material's ultra-low ionic conductivity of 3.21×10^{-10} S cm^{-1} at 65 ℃ in the ordered crystalline state (Fig. 11). The bands at 3230, 3163 and 2941 cm^{-1} are associated with N−H stretching.[S4,S5] The peak at 3136 cm^{-1} is attributed to the C−H stretch of the triazole ring.[S6] In addition, the bands at 1533 and 943 cm^{-1} are assigned to the ring stretching and N−H out-of-plane bending of the 1,2,4-triazolium cations, respectively.[S6] The peaks at 1354, 1262, 1221, 1193, 1165, 1138, 1064, 1040, 1023, 903, 805, 740 and 659 cm^{-1} are associated with the $CF_3(CF_2)_3SO_3^-$ anions.[S7−S11] For instance, the sharp absorption bands at around 1262 and 1193 cm^{-1} may correspond to the SO_3 asymmetric stretching vibration.[S7,S8] This spectral feature is characteristic for a sulfonate anion strongly involved in a hydrogen bond.[S9] The peaks at 1064, 1040 and 1023 cm^{-1} are attributed to the SO_3 symmetric stretching vibration of sulfonate anions.[S7,S10] The peak at 1221 cm^{-1} may be due to the perfluorobutyl functional groups of **1**.[S7,S11]

Thermal analysis

The relatively large $\Delta S_{III \to II}$ of 26.0 J K^{-1} mol^{-1} (Fig. 3) implies that the ions in **1** have a large extent of orientational freedom in Phase II. Assuming that the configurational entropy is the most dominant contribution for solid-solid phase transitions, the entropy change can be approximated according to Equation (S1):

$$\Delta S = R \times \ln(n_1 / n_2) \qquad (S1)$$

where R is the universal gas constant (8.314 J mol^{-1} K^{-1}), and n_1/n_2 is the ratio of the number of orientational freedoms of constituent molecules in the high and low temperature phases, respectively.[S12,S13] A ratio of 22.8 is obtained for $\Delta S_{III \to II}$ and this value is considered to account for the change in the number of orientations of all ions at $T_{III \to II}$. Moreover, compared with imidazolium

methanesulfonate ($T_{mp} = 188$ ℃, $T_{II \to I} = 174$ ℃),[S14] **1** exhibits a similar melting point but a much lower solid-solid phase transition temperature ($T_{III \to II} = 76.8$ ℃, $T_{II \to I} = 87.2$ ℃).

During the cooling scan, three corresponding exothermic peaks were recorded in the DSC trace (Fig. 3). Firstly, **1** crystallizes at around 176.8 ℃ with a sudden release of latent heat, which is similar to some reported plastic crystals.[S15,S16] The crystallization results in a slightly increased sample temperature in the dynamic DSC experiment as a loop in the cooling curve is seen at the crystallization temperature. Furthermore, each of the two reversible heat anomalies at 76.8 ℃/47.2 ℃ and 87.2 ℃/86.6 ℃ (on heating/cooling) displays a well-shaped peak on the DSC curve and a temperature hysteresis, proving the transformations of phase III → phase II and phase II → phase I are both first-order solid-solid phase transitions.[S17] DSC tests of **1** in the form of a pressed dense pellet (Fig. S6) or at a lower heating/cooling rate of 2 ℃ min^{-1} for fine powders (Fig. S7) are consistent with the DSC traces for fine powders of **1** recorded at 5 ℃ min^{-1} (Fig. 3).

Variable-temperature powder XRD analysis

To characterize the low temperature transitions at 76.8 ℃ and 87.2 ℃ as shown in the DSC trace (Fig. 3), fine powders of **1** were heated from 25 ℃ to 160 ℃ and the structural features were monitored by temperature-dependent powder XRD. As shown in Fig. 4, several diffraction peaks disappear or appear during the two endothermic transitions. When the sample was heated from 25 ℃ to 73 ℃, the powder XRD patterns were basically the same. From 74 ℃ to 78 ℃, two large reflections at $2\theta = 17.9°$ and $23.8°$ as well as some minor reflections at $2\theta = 11.4°$, $12.5°$, $14.2°$, $16.2°$, $18.5°$, $22.7°$, $27.6°$, $33.9°$, $34.6°$, $37.5°$ and $43.6°$ become weaker and disappear completely before 77 ℃ or 78 ℃. In particular, two major reflections at $2\theta = 29.7°$ and $35.8°$ diminish quickly and disappear completely at around 80 ℃, indicating clearly a transformation between two different crystalline structures and a likely increase in space group symmetry. These changes confirm the first endothermic transition (phase III → phase II), whose onset temperature is 76.8 ℃ and peak temperature is 78.4 ℃, to be a solid−solid phase transition. This phase transition is accompanied by an evident entropy change, $\Delta S_{III \to II}$, of 26.0 J K^{-1} mol^{-1}.

Meanwhile, starting from 74 ℃, several new reflections emerge at 2θ = 13.8 °, 16 ° and 19.5 ° and grow sharper and stronger at 85 ℃ while the weak diffraction peaks at 2θ = 17.4 ° and 32.3 ° vanish at about 82 ℃. From 81 ℃ to 85 ℃, obvious diffraction peaks at 2θ = 21.9 °, 27.4 ° and 32.9 ° begin to arise. In addition, weak diffraction peaks at 2θ = 16.5 °, 16.7 ° and 29.3 ° begin to appear at 82 ℃. From 85 ℃ to 160 ℃, the powder XRD patterns of the sample remain almost the same except a gradual shift in the peak positions toward lower 2θ values with increasing temperature due to continuous minor structural changes (*i.e.* thermal expansion of the lattice). Therefore, the second endothermic transition (phase II → phase I) at 87.2 ℃ in the heating scan of DSC trace is proved to be another solid−solid phase transition, though with a smaller entropy change, $\Delta S_{II \to I}$, of 5.35 J K^{-1} mol^{-1}. The slight difference in onset temperatures of lattice transformation and thermal transition should be related to the different heating methods for powder XRD and DSC measurements.[S14] The sharp reflections suggest that **1** possess long-range-ordered structures in phase I, II and III. While all of the diffraction peaks belong to the room temperature (phase III) powder XRD pattern completely disappear in phase I (the highest temperature solid phase), the powder XRD patterns of phase I are observed to be simpler, implying a more symmetric lattice system and phase I as a plastic phase.[S12,S14,S15,S17−S23] The reduction of diffraction peaks in phase I indicates the presence of dynamic rotational disorder which leads to the plastic properties. In addition, the increased rotating motion of ions increases the thermal factors of the atoms in the lattice and prevents diffraction in the high-2θ-angle region (e.g., $2\theta > 35$ ° above 82 ℃ as shown in Fig. 4).[S23]

Furthermore, Fig. S9 compares the powder XRD patterns of a pressed cylindrical dense pellet and fine powders of compound **1** at 25 ℃. The pellet was formed by uniaxial pressing of fine powders. While the fine powders show relatively clear and well resolved Bragg reflections with a weak diffuse background, the dense pellet shows an increase in intensity of the diffuse scattering background and an alteration in peak intensities, which might indicate the disorder.[S24,S25] When the temperature goes up to 160 ℃ (Fig. S10), the fine powders exhibit disorder as evidenced by the amorphous type diffraction which underlies the peaks.[S24] Meanwhile, the pellet displays simpler powder XRD patterns (*vs*. Fig. S9a and S10b) with remarkable alteration in peak intensities and some peaks

6

missing, again suggesting stronger rotational disorder in the plastic phase (phase I), which corresponds to the increased ionic conductivity (Fig. 11).

Single-crystal XRD analysis

The geometry of the anion (Fig. 7) is not linear as one may expect for a *n*-butyl chain as can be seen by the torsion angles along the chain (e.g., S6−C10−C13−C16 = −162.1(2)° at −173 ℃ and −170.5(6) °at 27 ℃; C10−C13−C16−C19 = −162.6(3)° at −173 ℃ and −174.6(12) °at 27 ℃).

It was also attempted to record single-crystal XRD data above 27 ℃ and above the transition temperatures of phase III → phase II and phase II → phase I. Above 27 ℃, the thermal motion of the perfluorobutyl chains increased further and made the structure refinements of very poor quality. Above the transition temperature of phase III → phase II, it was evident that the recorded diffraction patterns were no longer of single crystals so no structural information could be obtained.

Section 3: Supplementary Figures
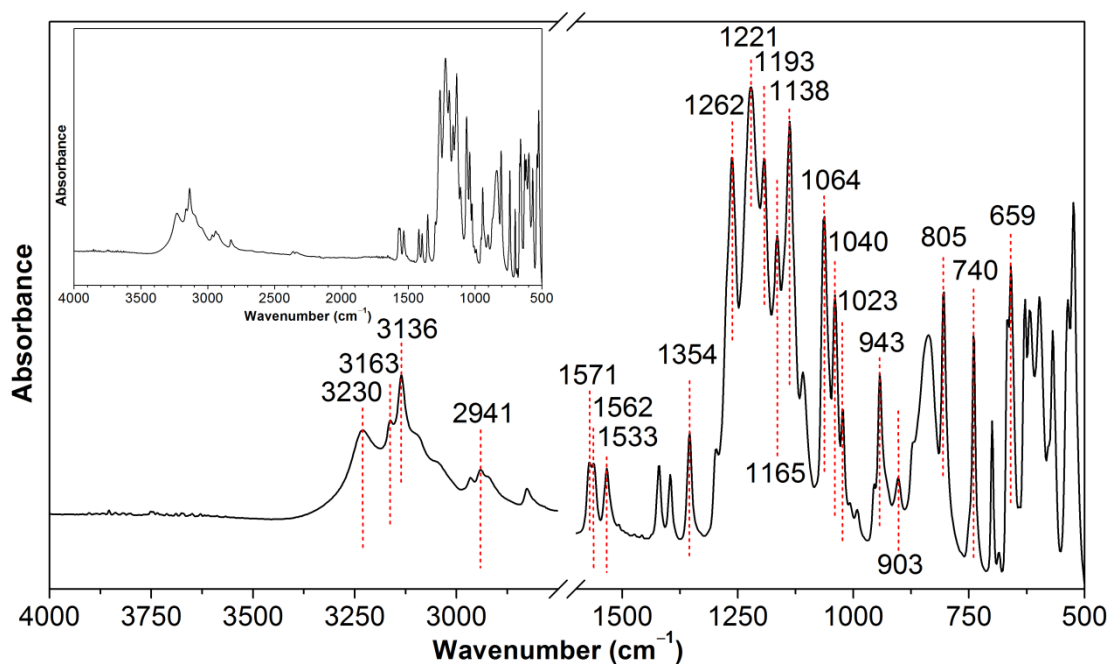
Fig. S1. FT-IR spectrum of powders of compound **1** recorded on a Bruker VERTEX 70 FT-IR spectrometer with an ATR accessory at room temperature. The inset is the complete IR spectrum, showing the absence of the H−O−H bending band of water at ~1650 cm^{-1}.
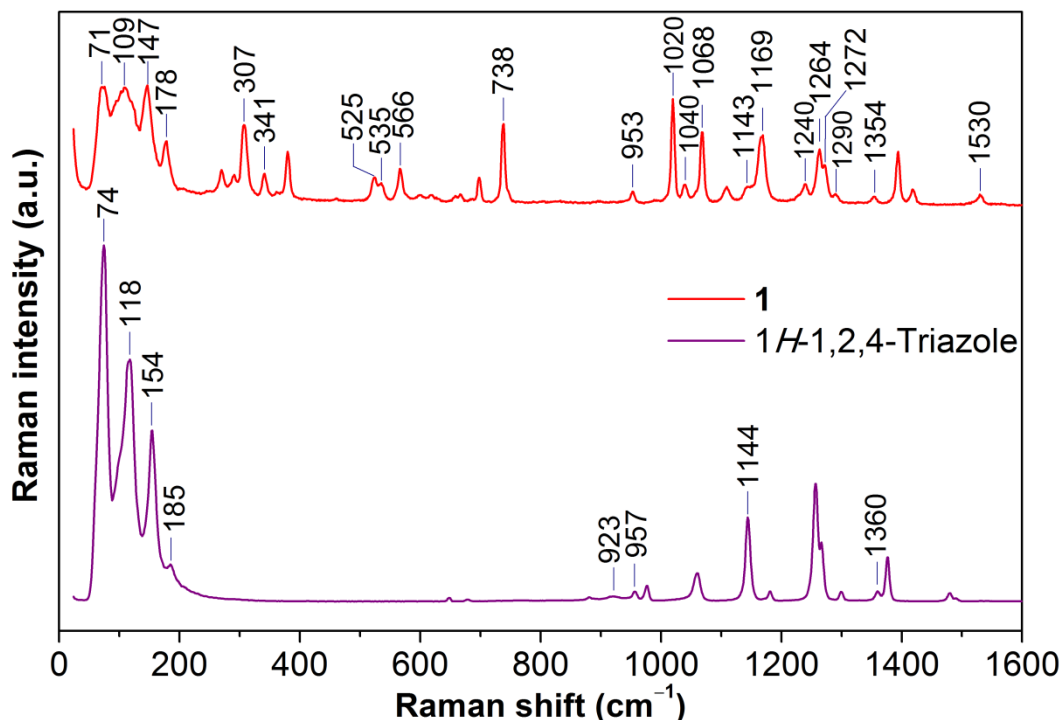
Fig. S2. Raman spectra of **1** in the form a pressed thin-film pellet (top curve) and 1*H*-1,2,4-triazole in the form of a plate (bottom curve) at 30 ℃. Data were recorded on a WITec Project system using a 785 nm excitation laser line. No traces of 1*H*-1,2,4-triazole have been detected in the Raman spectrum of **1**.

8
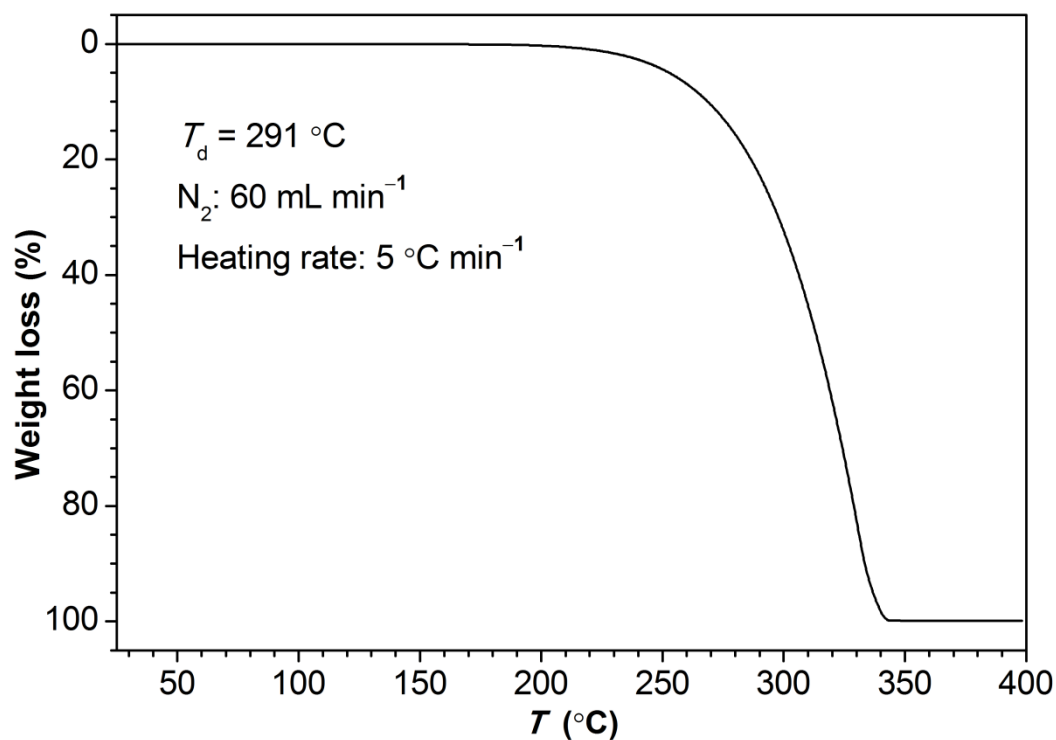
Fig. S3. Thermogravimetric analysis (TGA) of **1** recorded in a nitrogen atmosphere (60 mL min^{-1}) at a heating rate of 5 °C min^{-1}. The onset temperature of weight loss was used as the decomposition temperature (T_d). The one-step weight loss process also confirms the high purity of **1**.
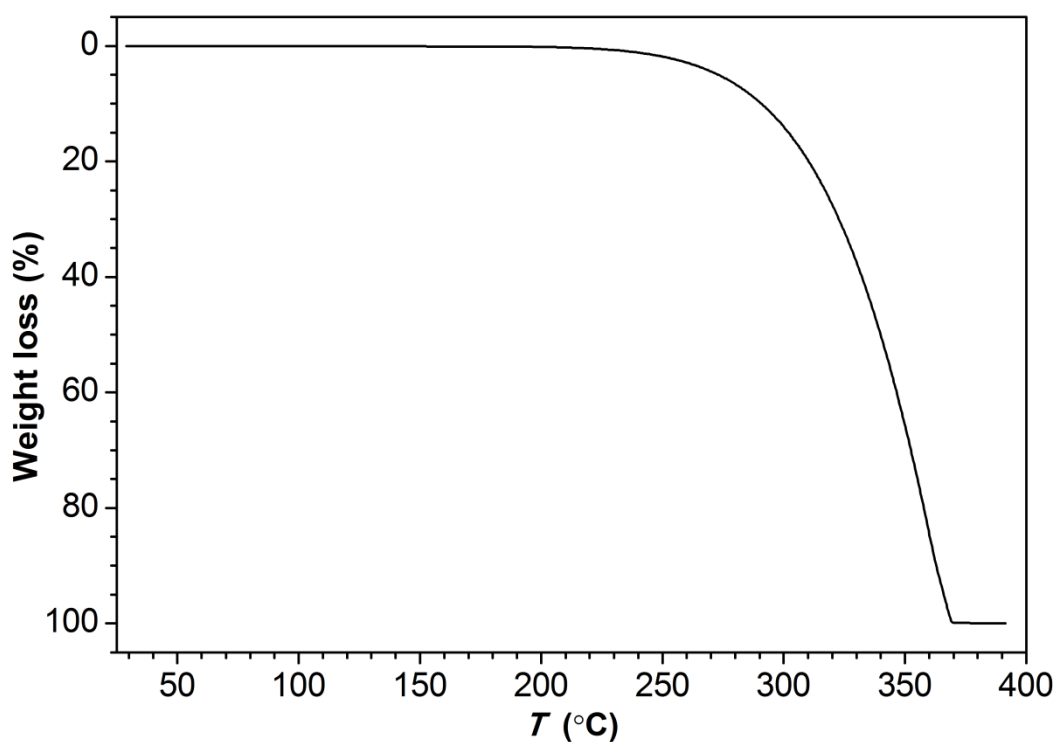
Fig. S4. TGA trace of **1** recorded in an air atmosphere (60 mL min^{-1}) at a heating rate of 10 °C min^{-1}, indicating that compound **1** is thermally stable in air.
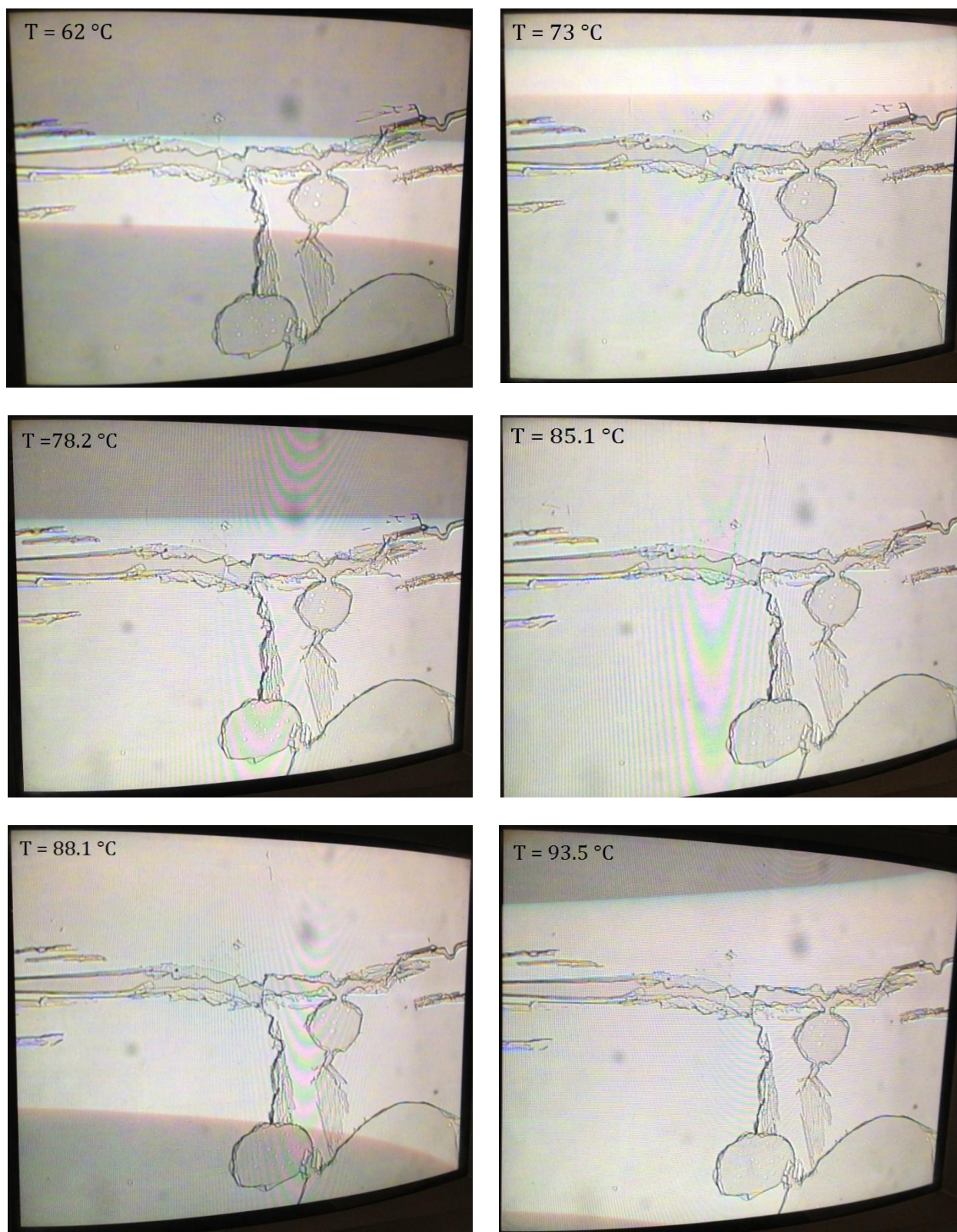
Fig. S5. Polarized optical microscopic images for powders of compound **1** placed between two glass plates during reheating from room temperature (phase III) to phase I, excluding the possibility of partial melting of **1** at around 77 ℃ and 87 ℃. The heating rate was 10 ℃ min^{-1}. Pictures were taken of the instant images shown on a Sony Trinitron monitor by using an iPhone 4S camera.
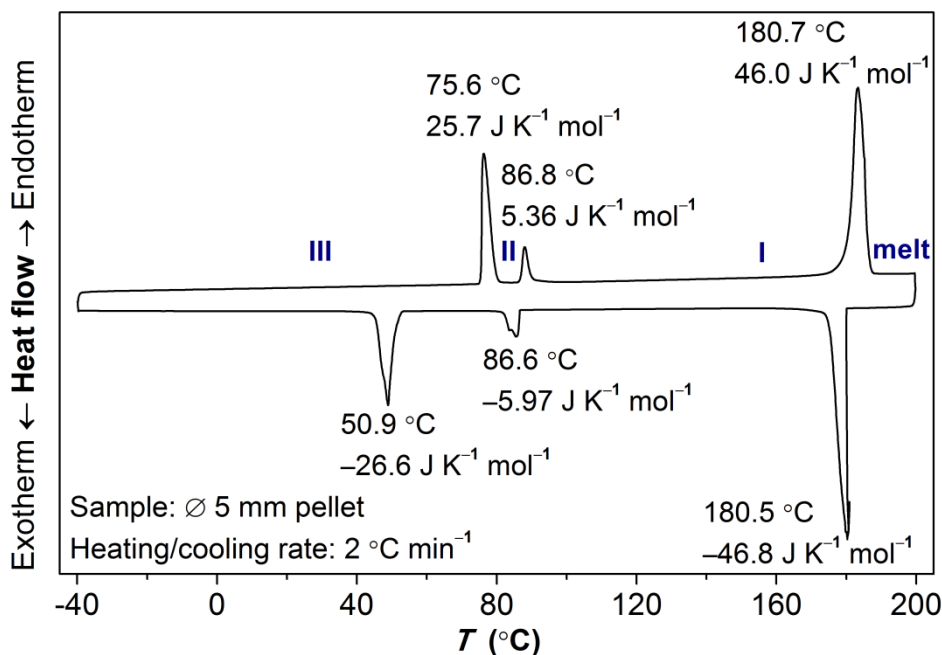
Fig. S6. DSC curves of **1** in the form of a pressed dense pellet with a diameter of 5 mm (sample mass: 45.37 mg). The onset temperatures and entropy changes for each phase transition are given. The heating/cooling rate was 2 °C min^{-1}. *The pellet is expected to have better contact with aluminum hermetic pans during DSC measurements than fine powders.* The sudden release of latent heat during the solidification is also seen for **1** in the form of a pressed dense pellet.
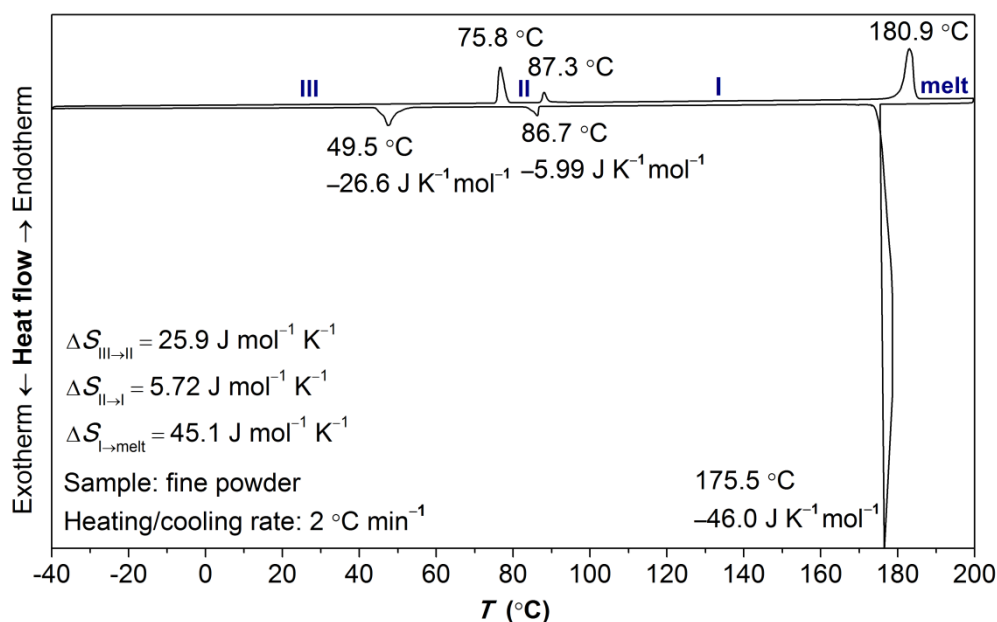

Fig. S7. DSC curves of **1** in the form of fine powders (sample mass: 19.47 mg) at a heating/cooling rate of 2 °C min^{-1}. The onset temperatures and entropy changes for each phase transition are given. Similar to **Fig. 3** and **Fig. S6**, the sudden release of latent heat during the solidification is also seen for **1** at a lower cooling rate. Again, the crystallization results in a slightly increased sample temperature in the dynamic DSC experiment as a loop in the cooling curve is seen at the crystallization temperature.
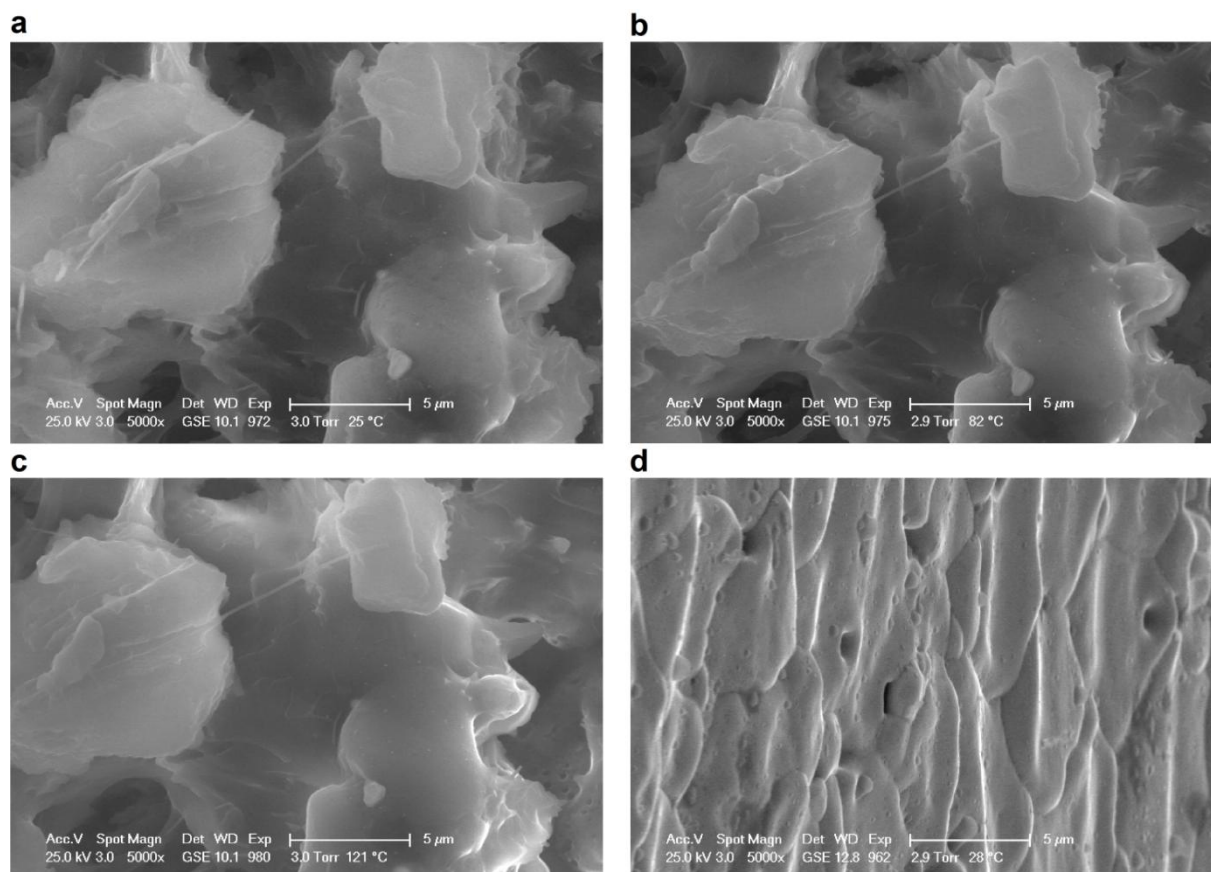
11

Fig. S8. SEM images of a plate, which was formed by natural solidification of melts of **1** in air. Images were acquired at different temperatures under a vacuum of around 3.0 Torr (*i.e.* ~400 Pa) with an acceleration voltage of 25.0 kV. Slip planes and steps on the fracture of the plate at (a) 25 ℃, (b) 82 ℃ and (c) 121 ℃, corresponding to phase III, II and I, respectively. (d) Slip planes appearing at the surface of the plate at 28 ℃. The holes are probably due to gas bubbles.
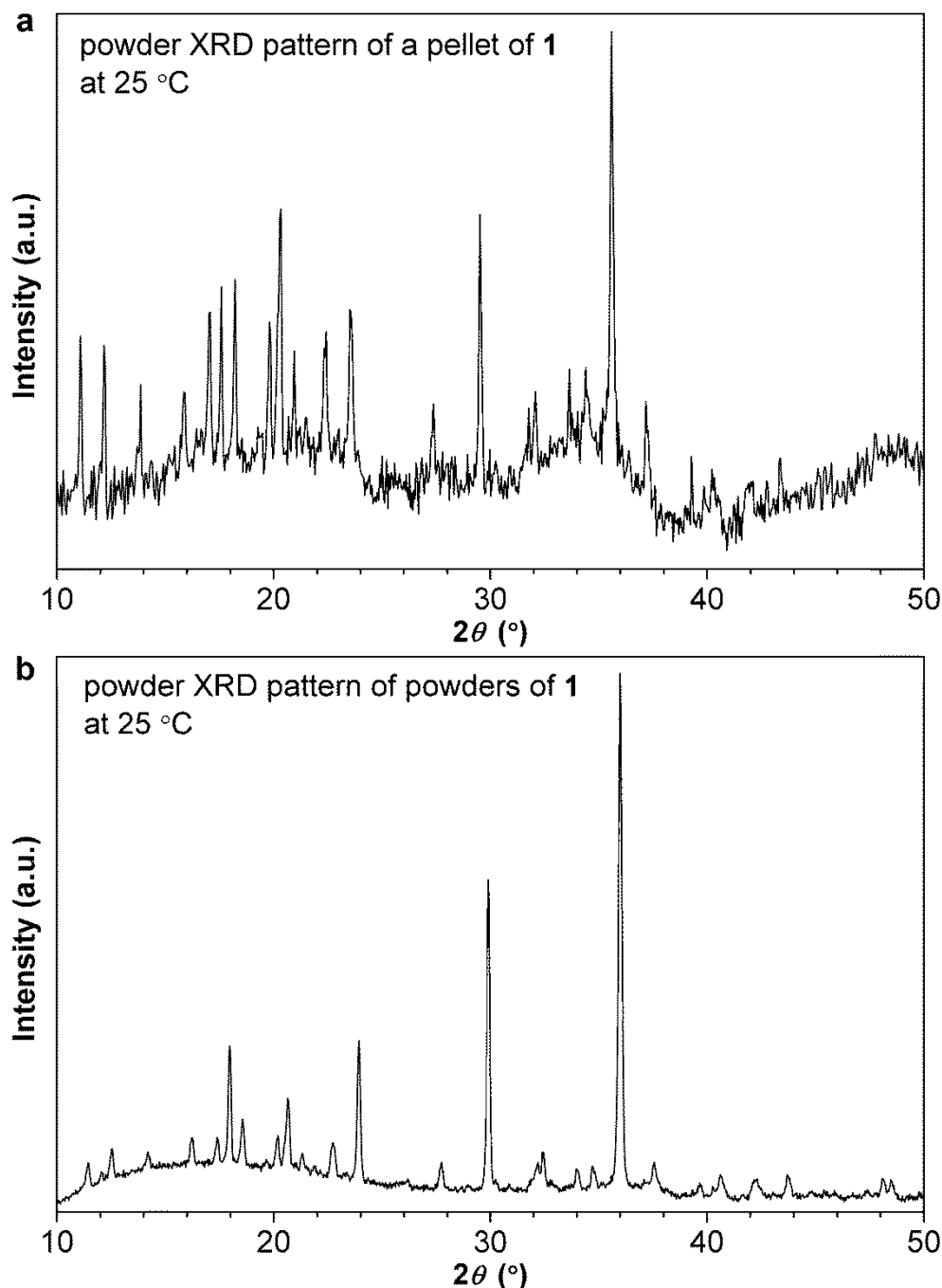
Fig. S9. Powder XRD patterns of (a) a pressed cylindrical dense pellet and (b) fine powders of compound **1** at 25 °C. The cylindrical dense pellet was prepared by uniaxial pressing of fine powders of **1** in a 10 mm diameter metal die under 20 kN (corresponding to a pressure of 255 MPa) for 1 min. Measurements were done in a high-temperature oven chamber (HTK 1200N, Anton Paar) with Ar atmosphere. The overall shift to higher 2θ values (also in **Fig. S10**) for peak positions of fine powders compared with those of the pressed dense pellet is most likely due to the error of height adjustment before measurement. The same X-ray diffractometer (X'Pert PRO, PANalytical) using Cu Kα radiation ($\lambda = 1.5406$ Å) was employed. Measurements were done in the same high-temperature oven chamber (HTK 1200N, Anton Paar) with argon atmosphere. Step size: (a) 0.052 °; (b) 0.026 °. Scan speed: (a) 0.039 °s^{-1}; (b) 0.011 °s^{-1}.
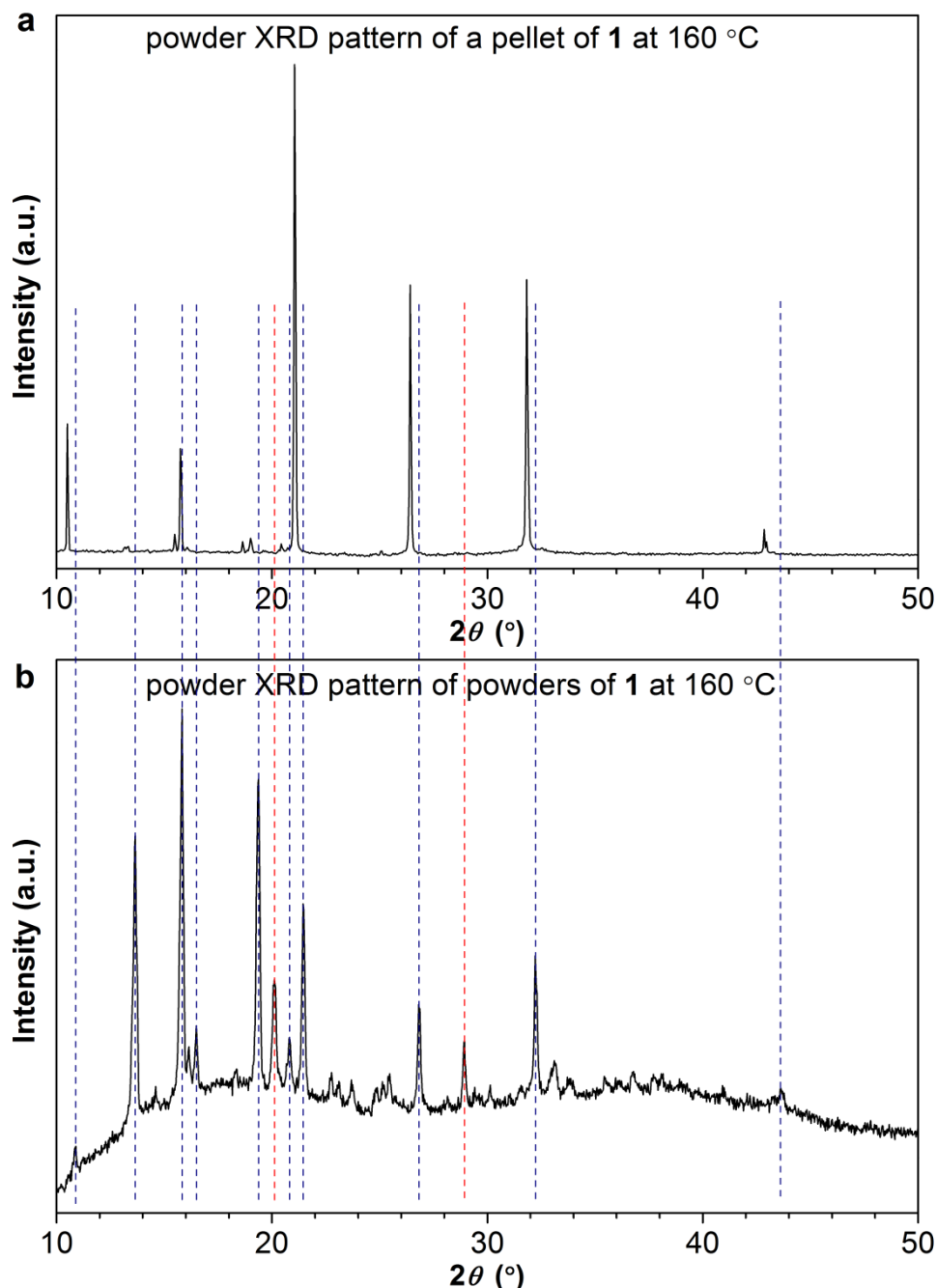
Fig. S10. Powder XRD patterns of (a) a pressed cylindrical dense pellet and (b) fine powders of compound **1** at 160 ℃ after the measurements at 25 ℃ shown in **Fig. S9**. The overall shift to higher 2θ values for peak positions of fine powders compared with those of pressed pellet is most likely due to the error of height adjustment before the measurement. It is clear that the reflections of fine powders of **1** include all of those of the pressed dense pellet of **1** with remarkable alteration in peak intensities and even some peaks missing (marked by red dashed line) in the latter. The fine powders exhibit disorder as evidenced by the broad amorphous type diffraction which underlies the peaks. The same X-ray diffractometer (X'Pert PRO, PANalytical) with Cu Kα radiation (λ = 1.5406 Å) was used. Measurements were done in the same high-temperature oven chamber (HTK 1200N, Anton Paar) with argon atmosphere. Step size: (a) 0.052 °; (b) 0.026 °. Scan speed: (a) 0.039 ° s^{-1}; (b) 0.011 ° s^{-1}.

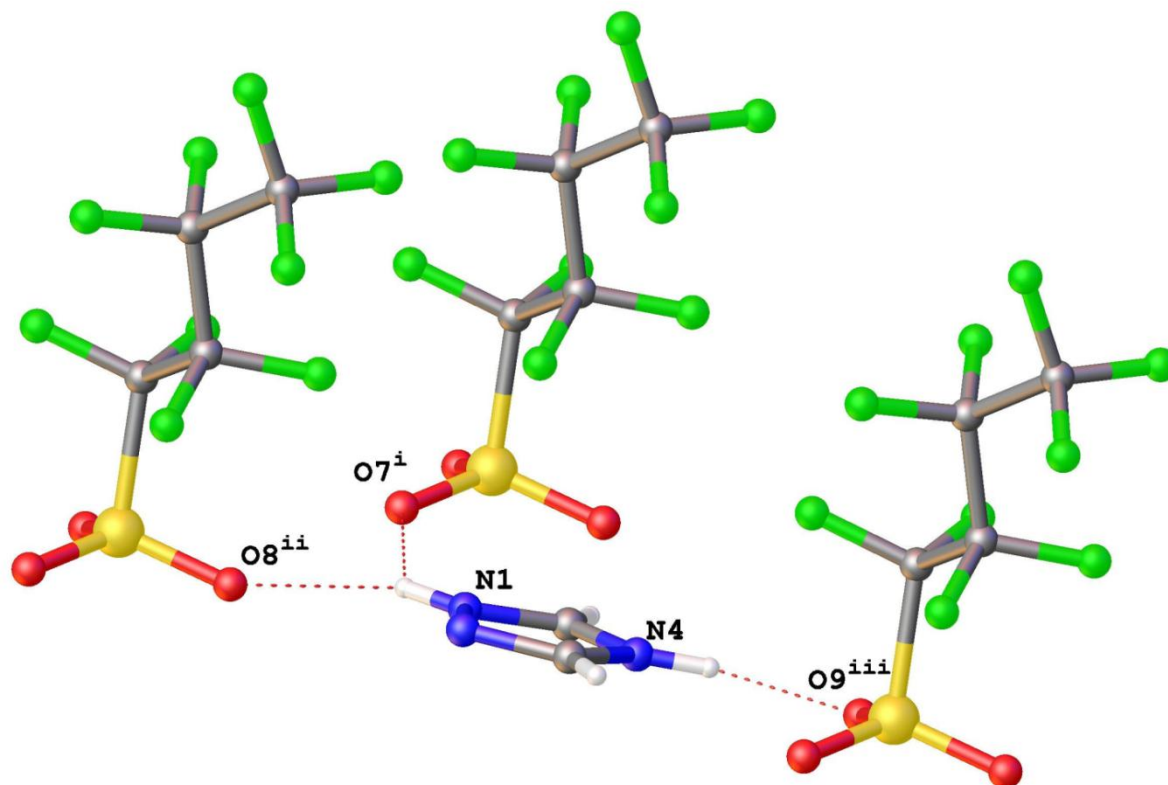**Fig. S11.** View of the crystal structure of **1** at −173 °C showing the hydrogen bonds between one 1,2,4-triazolium cation and three neighbouring perfluorobutanesulfonate anions (symmetry codes: *[i]* −1+x,−1+y,z; *[ii]* x,−1+y,z; *[iii]* −1+x,y,z).

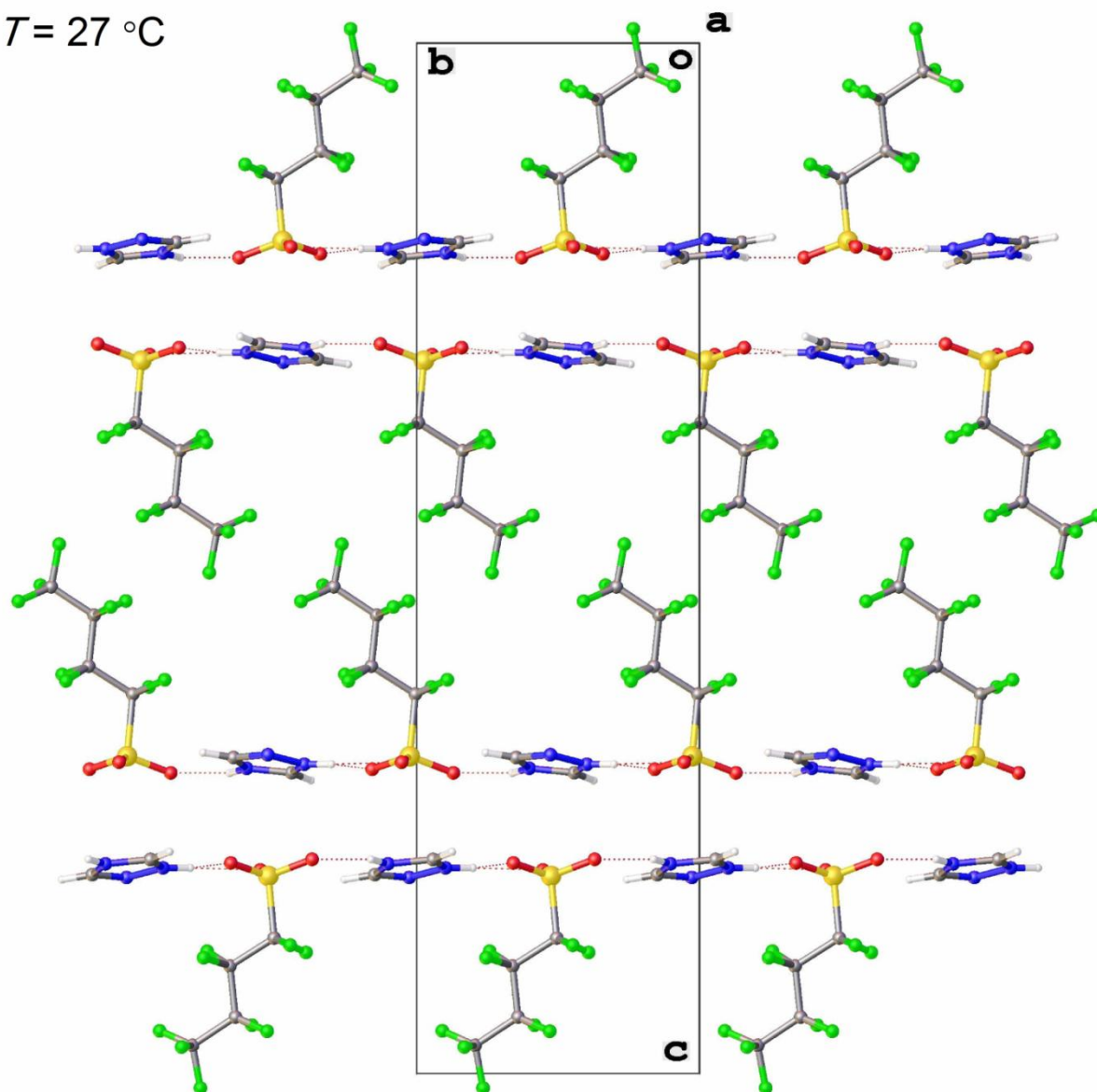**Fig. S12.** View of the packing in the crystal structure of **1** at 27 °C (C: grey; H: white; F: green; N: blue; O: red; S: yellow).
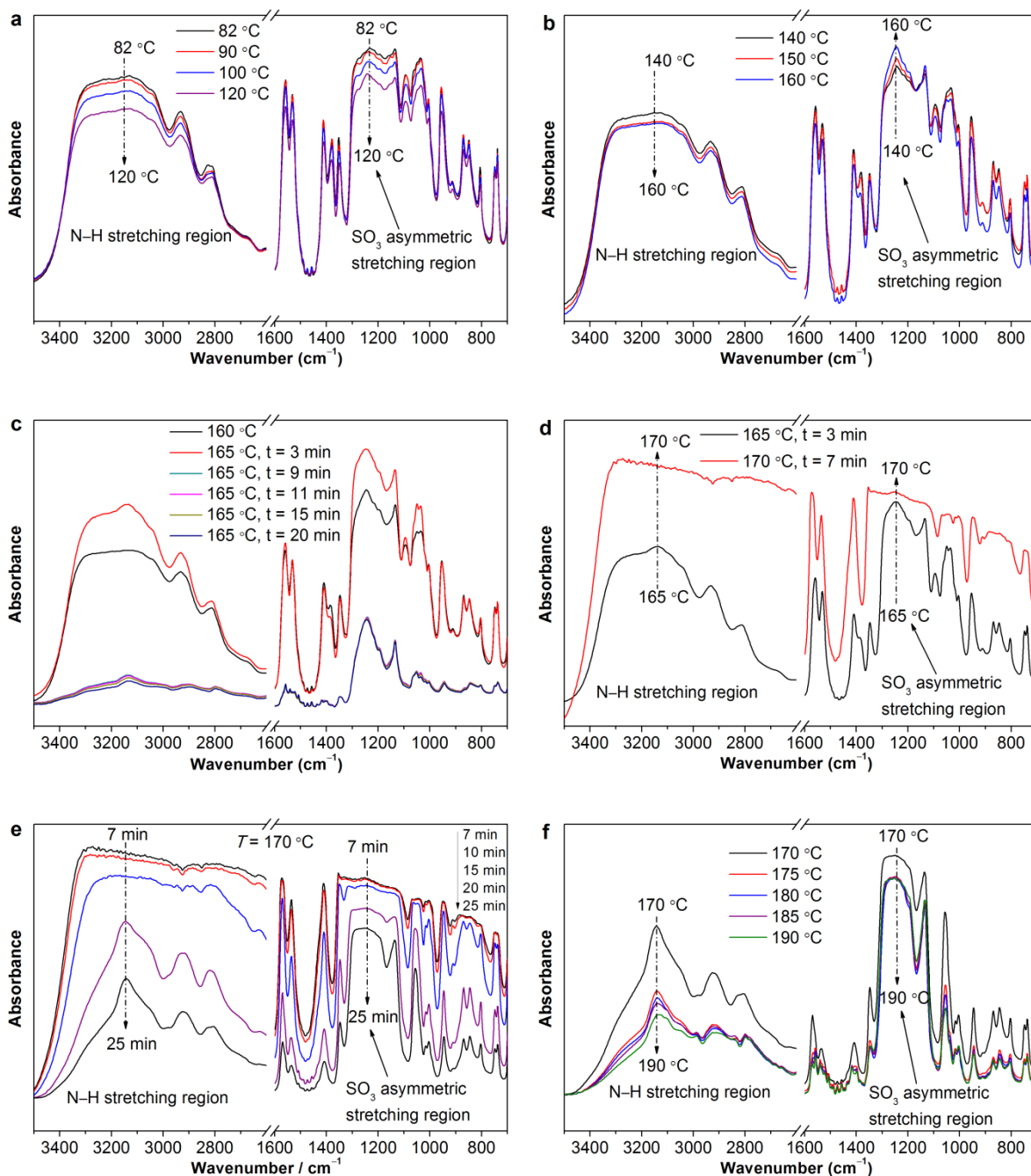
Fig. S13. Variable-temperature FT-IR spectra of **1** in the temperature range of 82−190 °C: (a) 82−120 °C; (b) 140−160 °C; (c) the evolution of the IR spectrum of the sample when the temperature reached 165 °C for 3, 9, 11, 15, and 20 min; (d) the IR spectra of the sample when it was heated at 165 and 170 °C for 3 and 7 min, respectively; (e) the evolution of the IR spectrum of the sample when the temperature reached 170 °C for 7, 10, 15, 20 and 25 min; (f) 170−190 °C. The sample was thermally equilibrated at each temperature for at least 15 min (unless otherwise specified) prior to the measurements. The heating rate was 1 °C min^{-1} between two consecutive temperatures. Note that the IR spectra of the crystal of **1** at temperatures ≤ 160 °C were stable and did not change with time. As from 165 °, the sample was no longer a single crystal (**Fig. S17** and **S18**).
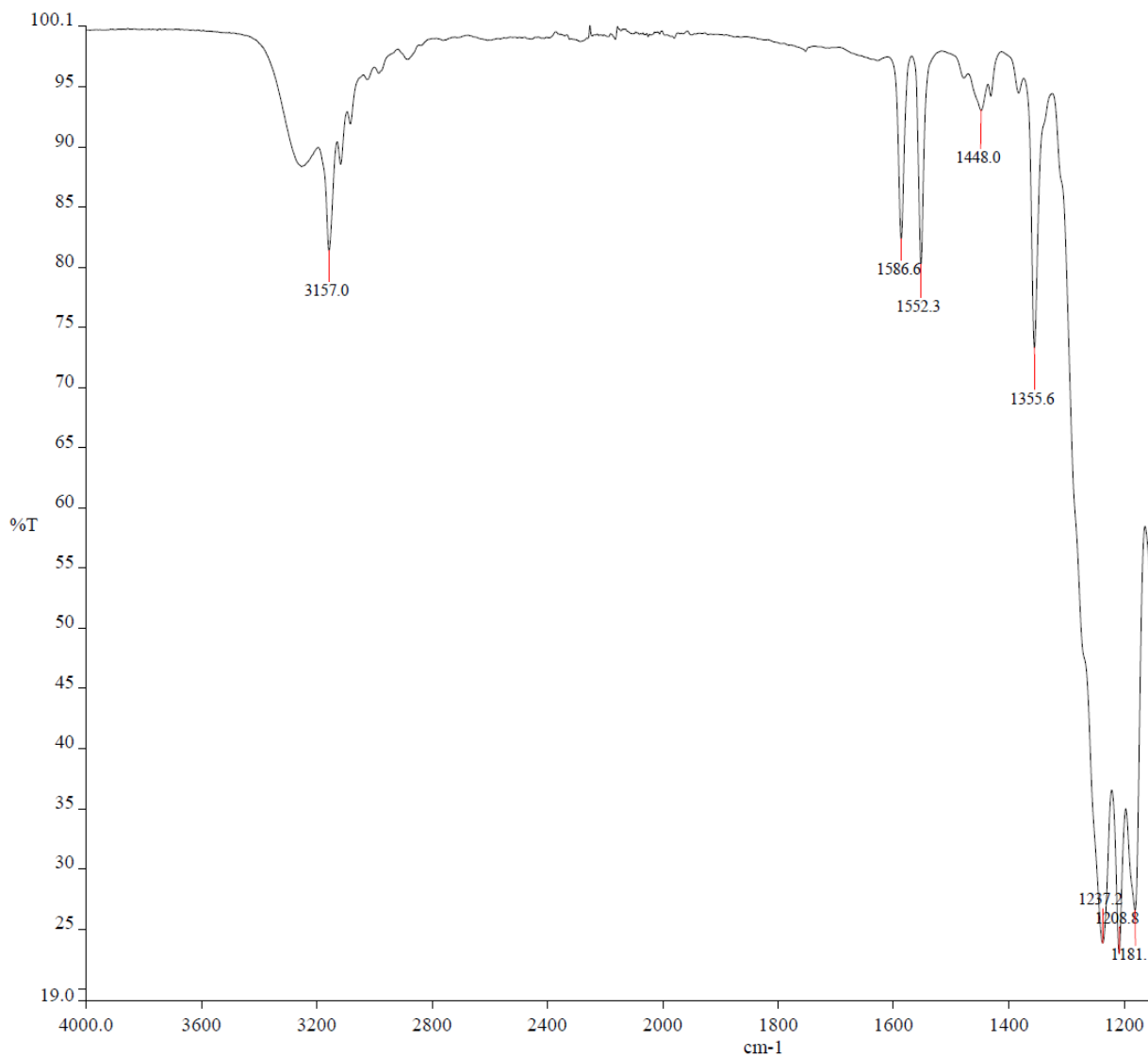
Fig. S14. FT-IR spectrum of 1-methylimidazolium perfluorobutanesulfonate at room temperature without exhibiting sharp vibrational modes at around 1419 and 1396 cm^{-1}. [S26]
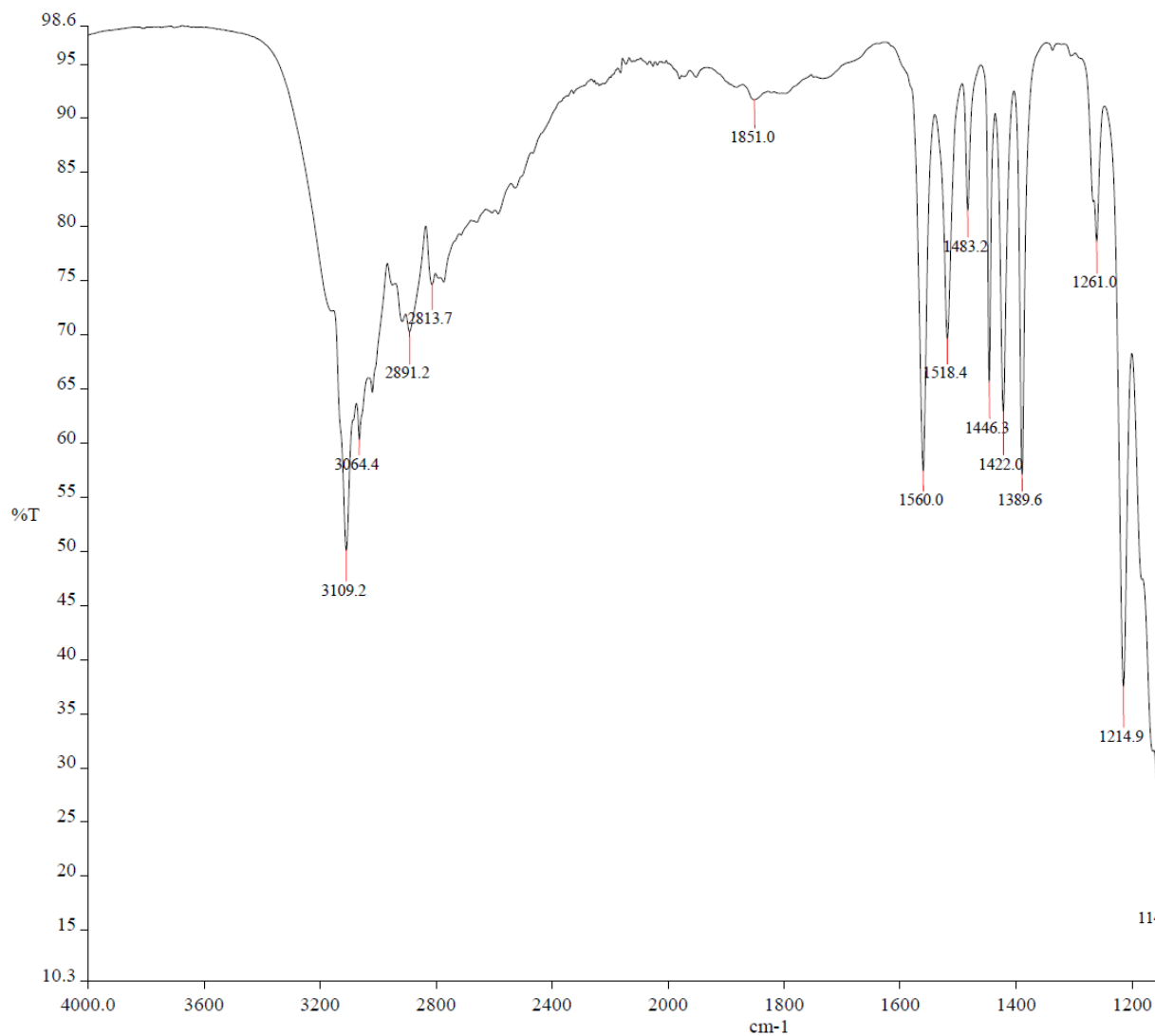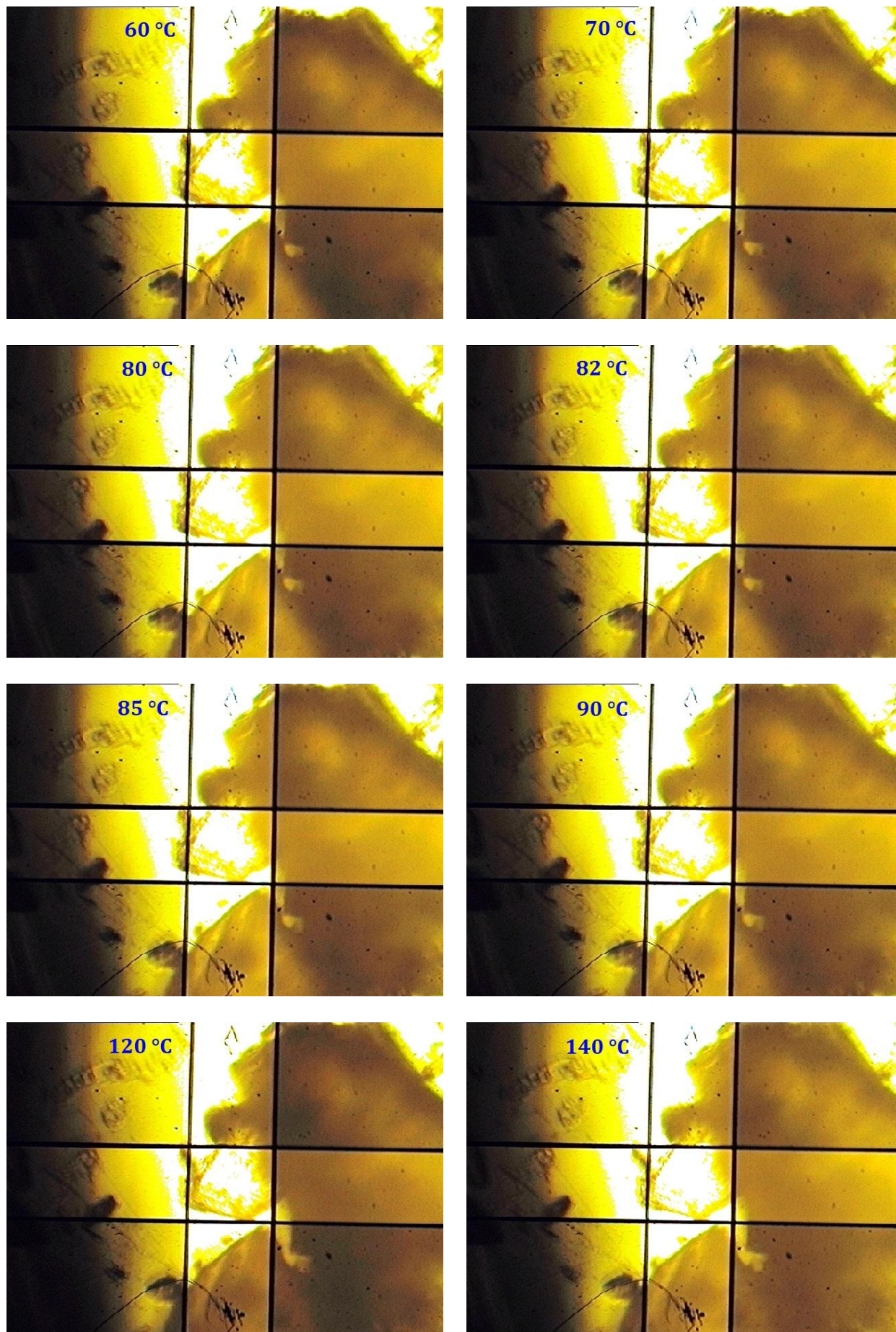
Fig. S15. FT-IR spectrum of 1,2,4-triazolium benzenesulfonate at room temperature, showing sharp vibrational frequencies at 1422 and 1390 cm^{-1}.[S26]
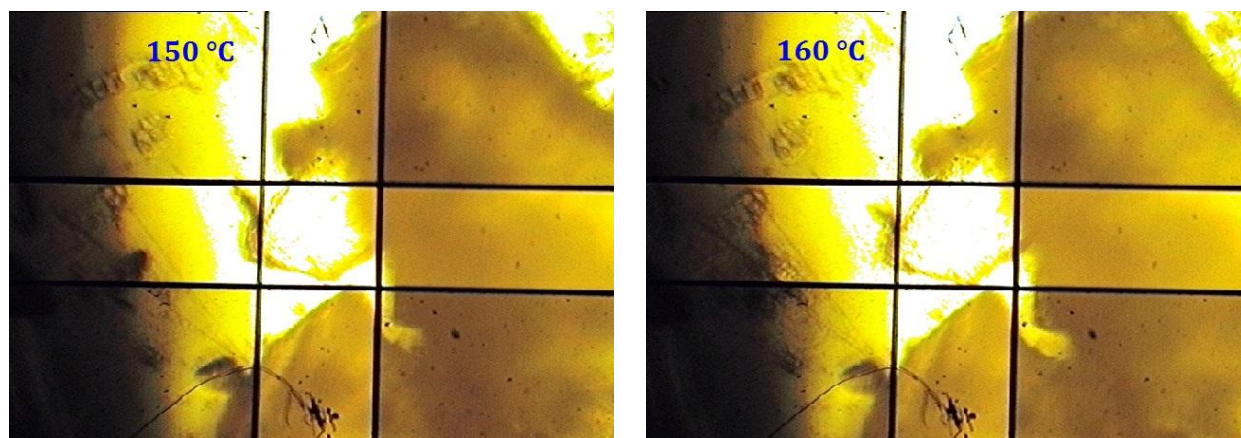
Fig. S16. Images of the single crystal recorded during variable-temperature FT-IR measurements at 60, 70, 80, 82, 85, 90, 120, 140, 150 and 160 °C, respectively. From 28 °C to 70 °C, the heating rate was 5 °C min^{-1} between two consecutive temperatures and was adjusted to 1 °C min^{-1} from 70 °C onwards. The sample was thermally equilibrated at each temperature for at least 15 min prior to the measurements. Images were taken by using the FT-IR imaging microscope (with a 15× objective lens) of Varian 670-IR FT-IR spectrometer. The crystal was in the central square.
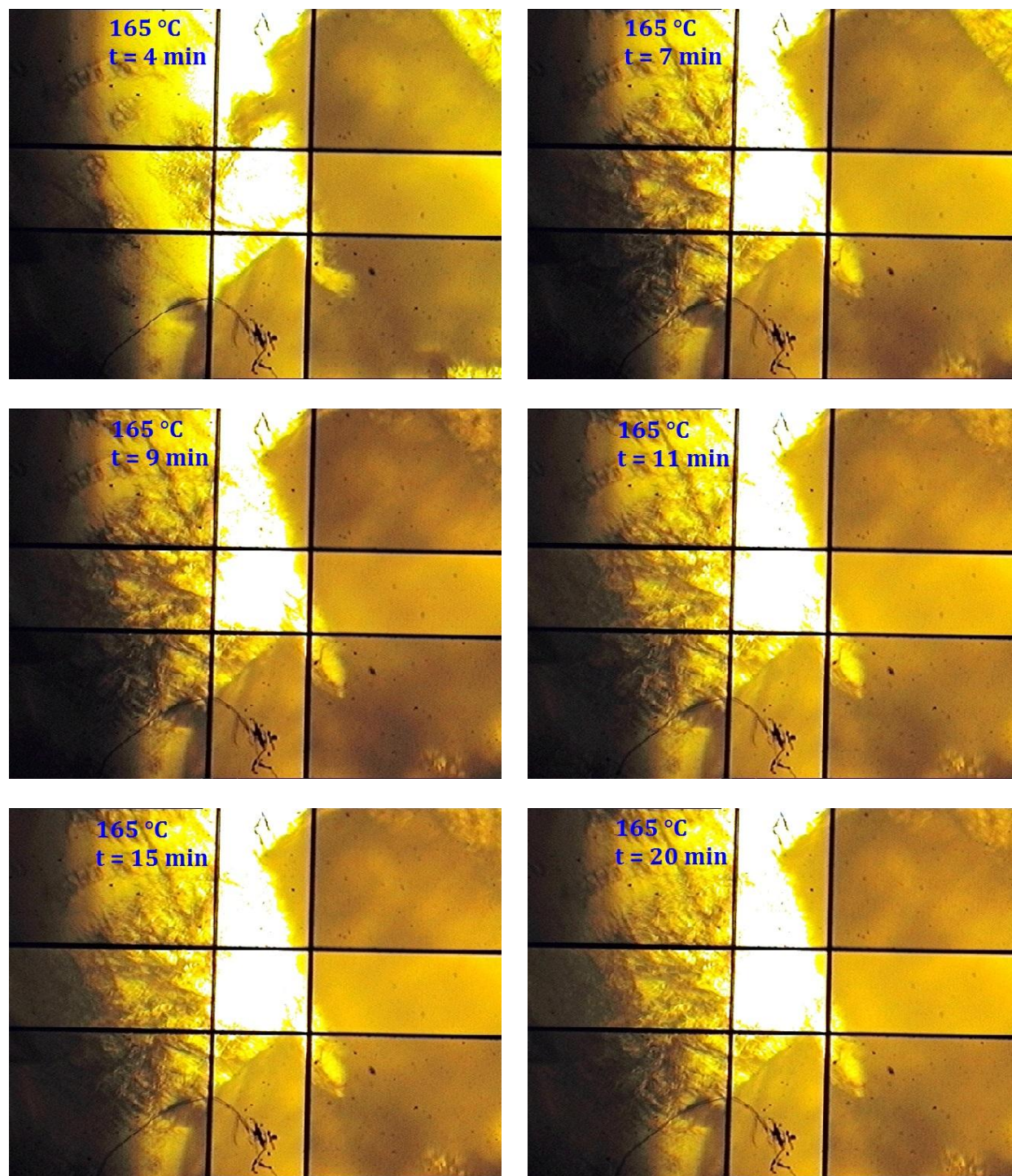
Fig. S17. The evolution of the optical microscopic images of the sample when the temperature reached 165 ℃ for 4, 7, 9, 11, 15, and 20 min. Images were taken by using the FT-IR imaging microscope (with a 15× objective lens) of Varian 670-IR FT-IR spectrometer. The sample, which was a crystal in the central square at the beginning, spreaded to its surroundings as if it flows. Together with Movie S1 showing the dynamic changes of the crystal of **1** heated at 165 ℃, the morphological changes upon heating from 160 ℃ to 165 ℃ may indicate a thermal-induced plastic flow. The seemingly "melting" process shown in the supplementary movie (**Movie S1**) is actually not a melting process. The exclusion of the "melting" is supported by the DSC (**Fig. 3**, **Fig. S6** and **S7**) and temperature-dependent powder XRD (**Fig. S18**) measurements for **1** as well as visual observations for a bulk sample of **1** during heating.
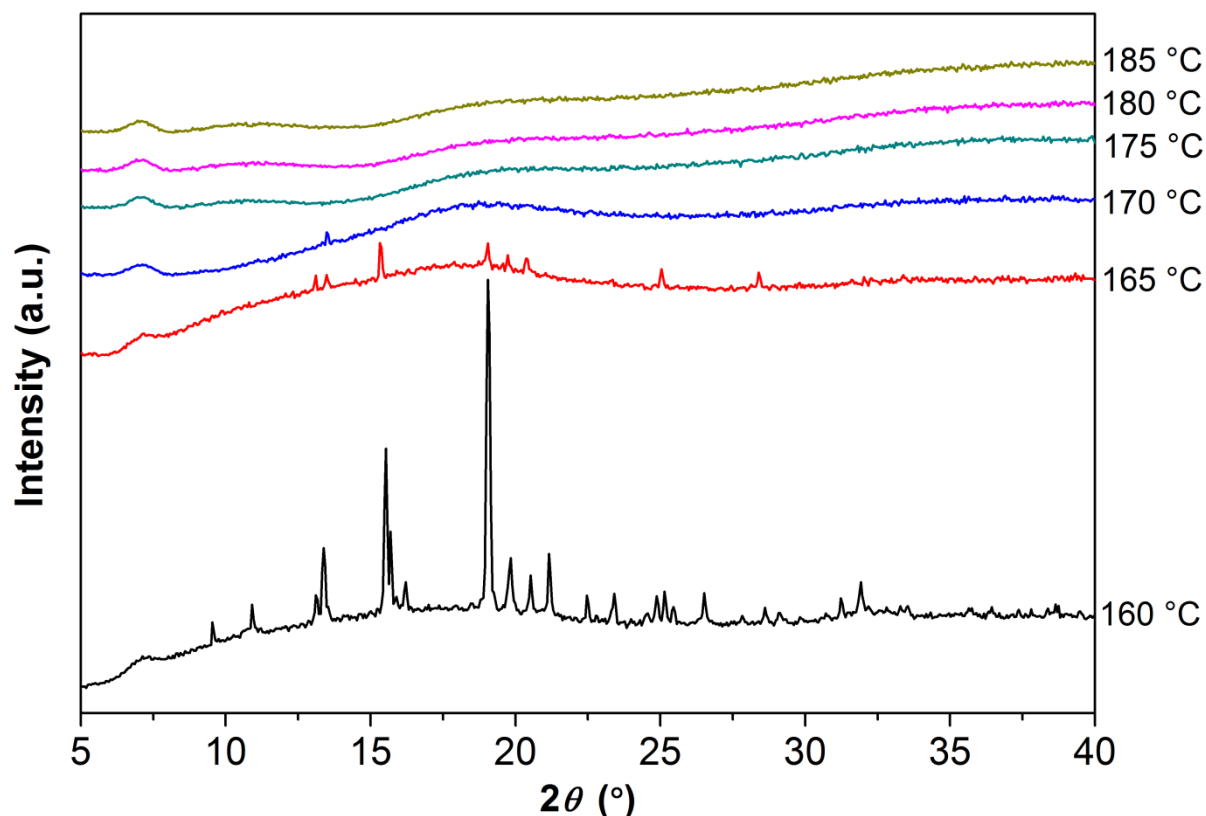
Fig. S18. Temperature-dependent powder XRD patterns of powders of **1** from 160 ℃ to 185 ℃ in an argon atmosphere. *The powders were used as synthesized (after purification) without being further ground into fine powders.* The sample was stabilized at each measurement temperature (accuracy: ±1 ℃) for about 20 min prior to the measurement. The temperature ramp between two consecutive temperatures was 5 ℃ min^{-1}. Measurements were carried out on a powder X-ray diffractometer (X'Pert PRO, PANalytical) using Cu Kα radiation (λ = 1.5406 Å). Each measurement consisted of a θ–2θ scan from 5° to 60° with a step size of 0.052° and a scan speed of 0.048° s^{-1}. Clearly, the sample began to lose its crystallinity at 165 ℃. At temperatures ≥ 170 ℃, it can be considered to be an amorphous material, implying the greatly increased disorder. Note that **1** melts at around 181 ℃. Importantly, visual observation confirms that **1** is still solid before 181 ℃.
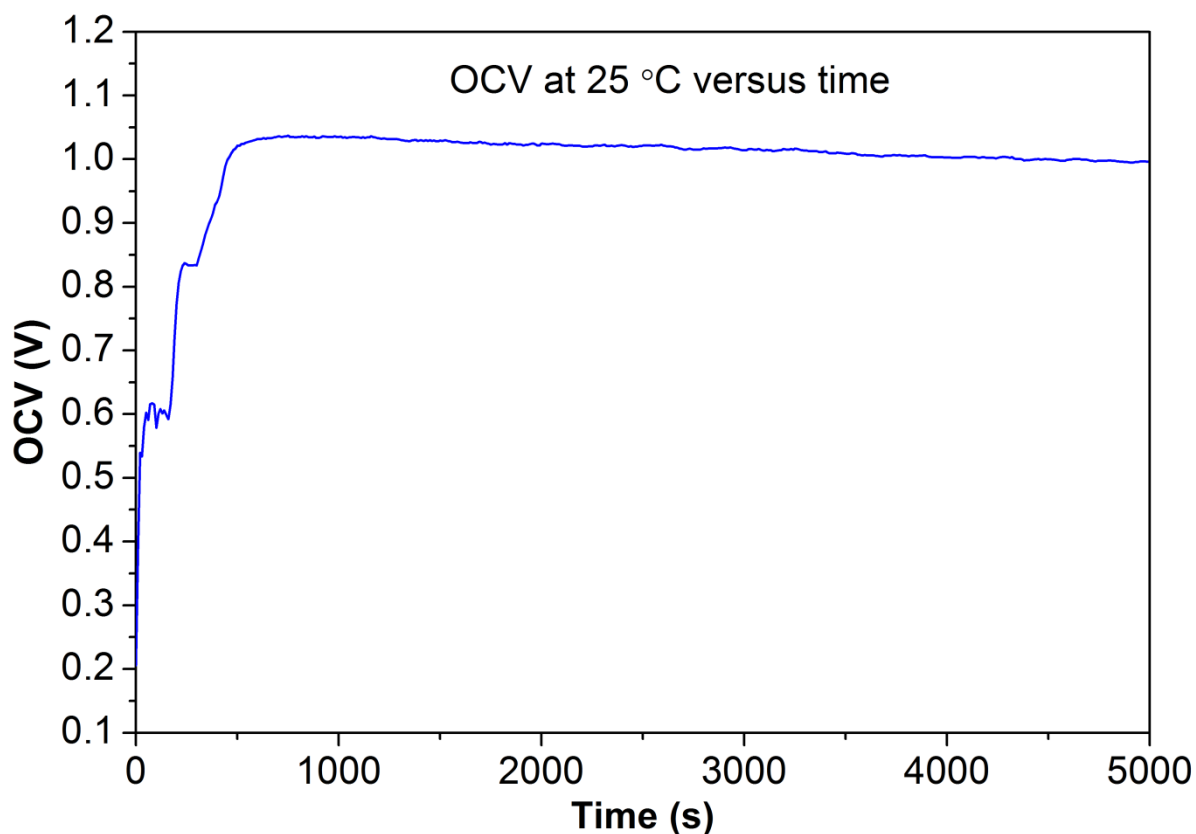
Fig. S19. OCV at 25 ℃ versus time evaluated using the following electrochemical cell: H_2, Pt/C|pressed pellet of powders of **1**|Pt/C, air. The gases were both dry. *The powders were used as synthesized (after purification) without being further ground into fine powders.* The fact that the OCV values were almost constant over 4000 seconds demonstrates the stability of the material in the dry hydrogen/air fuel cell environments. It should be noted that after grinding into fine powders, better OCV profiles are expected as evidenced in **Fig. 14b**, which is likely due to the resulting denser pellet as the elelectrolyte for fuel cells.

24

Section 4: Supplementary Table

Table S1. Fitting slopes of the polarization curves shown in Fig. 14a.

T/ °C	Slope/($M\Omega$ cm^2)[a]	R^{2} [b]	σ/(S cm^{-1})[c]
120	0.31262	0.958	3.1988×10^{-7}
130	0.17139	0.99021	5.8346×10^{-7}
140	0.09599	0.99658	1.0418×10^{-6}
150	0.05885	0.99886	1.6992×10^{-6}
160	0.05267	0.99698	1.8986×10^{-6}
170	0.05209	0.99929	1.9198×10^{-6}
180	0.01097	0.99806	9.1158×10^{-6}

[a] Slope = resistance $\times$ area, where area = 0.5 cm^2. [b] R^2: correlation coefficient. [c] $\sigma = d$/slope, where the thickness, d, of the cylindrical pellet is 0.10 cm.

We show that the direct current (DC) ionic conductivity of the pellet of the material in an operating fuel cell determined from the polarization curve agrees well with the alternating current (AC) ionic conductivity for a similar pellet of the POIPC **1**. This may be considered as additional proof that the material has significant proton conductivity, so that protonic conductivity constitutes the majority of the ionic conductivity in the lower plateau region (phase I, 100−155 °C). The reasons are explained as follows:

(a) Qualitatively, the very high open circuit voltage (OCV) (as high as 1.05 V at 150 °C) of our POIPC material provides evidence of long-range proton conduction. If we look at the principle of fuel cells, proton transfers across the "membrane" between anode and cathode is a vital process for the operating of fuel cells. As the OCV is high (approaching the theoretical value), that means the fuel cell reactions happen with long-range proton transfers from the anode to the cathode to complete the net reaction of "$H_2 + 1/2\ O_2 \rightarrow H_2O$". As the perfluorobutanesulfonate anions are unlikely to contribute to the current during fuel cell operation, the current should be contributed by the cations. No matter whether the cations move with 1,2,4-triazole as a vehicle for protons (vehicle mechanism), or the protons themselves hop (Grotthuss mechanism or structural diffusion), they both result in proton conduction. Hence, high OCV values are strong evidence of protonic conductivity and protons (including 1,2,4-triazolium cations) as the conducting species.

(b) It is well know that there are typically three factors influencing the fuel cell polarization curves: kinetic loss, ohmic loss (cell resistance), and mass transport loss.[S27] During the fuel cell test, the polarization curves were measured from 120 °C to 180 °C by linear sweep voltammetry at a scan rate of 10 mV s^{-1}, using the following electrochemical cell: H$_2$, Pt/C|cylindrical dense pellet of compound **1**|Pt/C, air. The pellet had a diameter of 13 mm and a thickness of 1.0 mm. As the electrodes are gas diffusion electrodes and the current densities are very low, the mass transport can be neglected. From the low AC ionic conductivity (Fig. 11), we know that the resistance of the pellet as a thin film electrolyte constitutes the absolute majority part of the cell resistance (pellet, anodes, cathodes, lines and so on). While the resistance of the 1.0 mm thick pellet can be as high as a few tenths of mega ohm, even the electrochemical reaction resistance (*i.e.* charge transfer resistance R_{ct}, which contributes to the kinetic loss) can be neglected when we consider the large resistance of the pellet film and the high open circuit voltage of the single fuel cells. Therefore, we may approximately estimate the DC ionic conductivity from the slopes of the polarization curves as shown in Fig. 14a and Table S1. It was then found that the obtained DC ionic conductivity agrees well with the AC ionic conductivity for a similar pellet of the material, confirming the dominate proton conductivity of the material.

Section 5: Supplementary Movie

Movie S1. The plastic flow of a crystal at t = ~3 min when it was heated at 165 ℃.

References

[S1] J. Luo, J. Hu, W. Saak, R. Beckhaus, G. Wittstock, I. F. J. Vankelecom, C. Agert and O. Conrad, *J. Mater. Chem.*, 2011, **21**, 10426.

[S2] J. Luo, T. V. Tan, O. Conrad and I. F. J. Vankelecom, *Phys. Chem. Chem. Phys.*, 2012, **14**, 11441.

[S3] J.-B. Brubach, A. Mermet, A. Filabozzi, A. Gerschel and P. Roy, *J. Chem. Phys.*, 2005, **122**, 184509.

[S4] E. S. Stoyanov, K. C. Kim and C. A. Reed, *J. Am. Chem. Soc.*, 2006, **128**, 8500.

[S5] M. S. Miran, H. Kinoshita, T. Yasuda, M. A. B. H. Susan and M. Watanabe, *Chem. Commun.*, 2011, **47**, 12676.

[S6] D. Bougeard, N. Le Calvé, B. Saint Roch and A. Novak, *J. Chem. Phys.*, 1976, **64**, 5152.

[S7] A. Bernson and J. Lindgren, *Solid State Ionics*, 1993, **60**, 37.

[S8] J. Luo, O. Conrad and I. F. J. Vankelecom, *J. Mater. Chem.*, 2012, **22**, 20574.

[S9] R. Langner and G. Zundel, *J. Chem. Soc., Faraday Trans.*, 1998, **94**, 1805.

[S10] C. M. Burba, N. M. Rocher, R. Frech and D. R. Powell, *J. Phys. Chem. B*, **2008**, **112**, 2991.

[S11] S. A. Forsyth, K. J. Fraser, P. C. Howlett, D. R. MacFarlane and M. Forsyth, *Green Chem.*, 2006, **8**, 256.

[S12] K. Kuchitsu, H. Ono, S. Ishimaru, R. Ikeda and H. Ishida, *Phys. Chem. Chem. Phys.*, 2000, **2**, 3883.

[S13] N. G. Parsonage and L. A. K. Staveley, *Disorder in Crystals*, Clarendon Press, Oxford, 1978.

[S14] J. Luo, O. Conrad and I. F. J. Vankelecom, *J. Mater. Chem. A*, 2013, **1**, 2238.

[S15] W. A. Henderson, V. G. Young, Jr., W. Pearson, S. Passerini, H. C. De Long and P. C. Trulove, *J. Phys.: Condens. Matter*, 2006, **18**, 10377.

[S16] F. Meersman, B. Geukens, M. Wübbenhorst, J. Leys, S. Napolitano, Y. Filinchuk, G. Van Assche, B. Van Mele and E. Nies, *J. Phys. Chem. B*, 2010, **114**, 13944.

[S17] P. Szklarz, A. Pietraszko, R. Jakubas, G. Bator, P. Zieliński and M. Gałazka, *J. Phys.: Condens. Matter*, 2008, **20**, 255221.

[S18] W. A. Henderson, D. M. Seo, Q. Zhou, P. D. Boyle, J.-H. Shin, H. C. De Long, P. C. Trulove and S. Passerini, *Adv. Energy Mater.*, 2012, **2**, 1343.

[S19] J. M. Chezeau and J. H. Strange, *Phys. Rep.*, 1979, **53**, 1.

[S20] J. Sun, D. R. MacFarlane and M. Forsyth, *Solid State Ionics*, 2002, **148**, 145.

[S21] R. Asayama, J. Kawamura and T. Hattori, *Chem. Phys. Lett.*, 2005, **414**, 87.

[S22] T. Enomoto, S. Kanematsu, K. Tsunashima, K. Matsumoto and R. Hagiwara, *Phys. Chem. Chem. Phys.*, 2011, **13**, 12536.

[S23] R. Taniki, K. Matsumoto, R. Hagiwara, K. Hachiya, T. Morinaga and T. Sato, *J. Phys. Chem. B*, 2013, **117**, 955.

[S24] D. R. MacFarlane and M. Forsyth, *Adv. Mater.*, 2001, **13**, 957.

[S25] J. Efthimiadis, S. J Pas, M. Forsyth and D. R. MacFarlane, *Solid State Ionics*, 2002, **154−155**, 279.

[S26] J. Luo, unpublished data, **2011**.

[S27] M. K. Debe, *Nature*, 2012, **486**, 43.